

An improved constitutive model for thixotropic elasto-viscoplastic suspensions of aggregating particles using population balances

Soham Jariwala, Rong Song, Julie B. Hipp, R. Bertrum Diemer, Antony N. Beris, Norman J. Wagner**

Soham Jariwala, Rong Song, R. Bertrum Diemer, Norman J. Wagner, Antony N. Beris

Center for Research in Soft matter & Polymers (CRiSP), Department of Chemical and Biomolecular Engineering, University of Delaware, Newark, Delaware, USA-19716

Corresponding authors: beris@udel.edu, wagnernj@udel.edu

Julie B. Hipp

Corporate Engineering, The Procter & Gamble Company, West Chester, Ohio, USA-45069

Abstract

An improved population balance-based rheological constitutive framework for polydisperse aggregating suspensions is derived by incorporating detailed models for orthokinetic and perikinetic aggregation and shear breakage processes. The framework accounts for critical properties such as dynamic arrest, viscoelasticity, kinematic hardening, thixotropy, and yield stress to generate a full range of thixotropic elasto-viscoplastic (TEVP) response. Additionally, the model is thermodynamically consistent because the dynamics and timescales are completely determined by internal structural and kinetic variables. The model connects the rheological response to the structural descriptors such as the size distribution of agglomerates, mean sizes, fractal dimension and agglomerate volume fraction. Predictions are compared against a wide range of shear rheology measurements data for model thixotropic suspensions of fumed silica and carbon black, including large amplitude oscillatory shear (LAOS), as well as ultra-small angle neutron scattering under steady shear (Rheo-uSANS). While the steady state fits and transient predictions suggest that the model accurately captures viscoelasticity and thixotropy at medium and large deformation rates, there is room for improvement in the elasto-viscoplastic modeling to enhance predictions for short time transients and small deformation rates.

Keywords: rheology, population balance modeling, thixotropy, colloids, suspensions

1. Introduction

Aggregating suspensions are common in consumer products as well as industrial processes.¹⁻⁴ These solid-liquid mixtures typically involve small particles (~ 10 nm – 1 μ m) suspended in a liquid formulation. Examples include paints, adhesives,⁵ printer inks, clay and ceramics,^{6,7} and even biological liquids such as blood⁸ and synovial fluid.⁹ These suspensions exhibit thixotropic, viscoelastic behavior and, in some cases, an apparent yield stress (see review by Mewis and Wagner for a detailed overview of thixotropic materials²). Consequently, developing modeling approaches for such suspensions is an active research aim.¹⁰⁻¹⁵

Of interest here are modeling approaches that represent explicitly the thixotropic, viscoelastic, and yielding (or thixotropic elasto-viscoplastic (TEVP)) behavior as a consequence of time and deformation dependent mesoscale structure of the solid phase. Three general approaches to this modeling can be identified as structure kinetics, physically-based population balance equations, and direct numerical simulation. Literature reviews (ref. Barnes,⁴ Mewis and Wagner,² Larson and Wei¹¹) and research monographs (ref. Ramkrishna,¹⁶ Wagner and Mewis,¹⁷ and Mewis and Wagner¹) provide background and historical context on the former two, while direct numerical simulation is necessarily limited in system size and complexity and often finds utility in testing specific physical processes, as will be illustrated in the following.

Large agglomerates form in such suspensions due to interparticle interactions (such as depletion, Van der Waals, and electrostatic), resulting in extra stresses of both viscous and elastic nature as these structures impart drag on the medium and form system-spanning networks. Such structures are deformation/stress sensitive and take finite time to deform, break, and aggregate, so that the suspension can exhibit viscoelasticity, thixotropy, and yield stress. This microstructural behavior manifests macroscopically as thixotropy, which is usually defined in terms of time-dependence of

viscosity,¹⁸ as well as viscoelasticity, arising from both Brownian motion of the particles (if they are colloidal in size) and stored elasticity in the microstructure itself. In order to distinguish between thixotropy and viscoelasticity from a microstructure point of view, we offer the following definition:

“Thixotropy refers to a history-dependent rheology due to the reversible breaking and reformation of physical or chemical bonds between constituent particles. It can clearly co-exist with viscoelasticity, which is due to conformational changes in the structure without breakage or reformation of bonds.”

This new definition emphasizes the central role of micro- and mesoscale structural changes, such as agglomerate aggregation-breakage processes and deformation to the time evolution of rheological behavior.^{19,20}

Chief among the modeling approaches for the aggregation and breakage behavior are structure kinetics models that involve scalar structure parameters, typically bounded between two extremes of fully “structured” and “unstructured” liquid.^{11,15,21} Following the original work of Goodeve,¹² a structure parameter is introduced as a loose analog of the degree of bonding between particles in the agglomerates. Recent versions of structure kinetics by Wei *et al.*²¹ and Varchanis *et al.*²² (ML-IKH and SPTT-IKH models, respectively) model TEVP physics and include phenomena such as isotropic and kinematic hardening, combining them with elasto-viscoplastic constitutive relationships such as those proposed by Saramito²³ and Phan-Thein & Tanner.²⁴ Although such representations demonstrably capture the viscoelastic and thixotropic phenomenology of these suspensions, the model construction is usually *ad hoc* and lacks a clear connection to measurable physical quantities. The problem of thermodynamic inadmissibility for this class of rheological constitutive equations has been addressed in the work by Joshi.²⁵

Recently, the use of population balance modeling has been proposed to address the criticism of structure kinetics modeling.²⁶ Population balance modeling provides a more direct representation of the kinetics of mesoscale structure evolution and also allows for the inclusion of additional particle-level phenomena such as diffusion and irreversible growth, which were absent from previous modeling paradigms. The historical importance of aggregation and breakage process is well documented.¹⁶ First serious effort in this direction can be attributed to Marian Smoluchowski who derived the master equation describing the population evolution as well as collision frequencies for Brownian and shear-driven aggregation.^{27,28} A rich body of work has emerged looking at the flocculation behavior of colloidal particles under various flow regimes owing to Smoluchowski's framework and the advancements in modeling colloidal interactions to overcome the limitations of the DLVO theory.²⁹ The collision efficiency and collision frequency of aggregating particles depend on the particle shape, size distribution, interaction, hydrodynamics, and flow regime. For a given collision environment (e.g., diffusion-limited vs. reaction-limited), a distinct colloidal population can form.³⁰ Due to the emergent nature of agglomerate morphologies, their shapes and conformations become challenging to describe; however, it is common to use fractal descriptions so that the morphological characteristics reduce to a single parameter, the fractal dimension.^{31,32} Although this description is limited, it adequately describes self-similar structures generated due to isotropic aggregation and breakage kinetics through scalar expressions.³²⁻³⁴ It has been observed that suspensions under shear can undergo alignment and compaction, with the fractal dimension evolving with deformation and time, and in some cases leading to the breakdown of self-similar and isotropic behavior.^{20,35} Here, population balance modeling can benefit from direct numerical simulations; using Dissipative particle dynamics (DPD), Jamali *et al.*²⁰ have elucidated the transient morphology of the agglomerates at various low and intermediate shear rates, showing the

emergent anisotropy, compaction and aging behavior, and identified the dyadic of center-to-center distance, or fabric tensor, to be a promising three-dimensional structural descriptor. Because it is based on actual physical processes described at the particle level, the inherent power of using population balance modeling as a framework for developing rheological constitutive equations is that rational and systematic improvements can be made. Additionally, parameters appearing in the modeling have physical meaning and, in principle, can be obtained independently and not necessarily fitted to the rheological behavior. In other words, unlike structure kinetics approaches which are inherently empirical, this modeling approach can be truly predictive. We demonstrate aspects of both of these distinct advantages in the work presented here.

Foundational work by Mwasame *et al.*²⁶ demonstrated that population balance modeling can be incorporated into a robust, efficient, and accurate rheological constitutive model. In that work, the model presented (hereafter referred to as PBEMono) used a monodisperse closure to develop the moment version of the population balance equation as a coarse-graining assumption. The use of a closure assumption for the moments of the size distribution enables reducing the inherent integro-differential nature of population balance equations to a finite system of simultaneous ordinary differential equations in time, similar in complexity, but distinct in form to the typical structure kinetics models (for a more detailed discussion, see Mwasame *et al.*²⁶). While successfully applied to model a range of thixotropic and viscoelastic behavior in suspensions of fumed silica and human blood,³⁶ the oversimplistic nature of the monodisperse assumption fails to adequately represent the agglomerate distribution and significantly overpredicts the agglomerate sizes when compared with independent microstructural measurements.³⁷ Polydisperse particles typically pack at a much higher volume fractions ($\phi_{\max}^{\text{mono}} < \phi_{\max}^{\text{poly}}$), and Mwasame *et al.*³⁸⁻⁴⁰ proposed corrections in relative viscosity relationships that can be directly incorporated into an improved approach. Importantly,

then, independent, verified studies of the effects of closure assumptions on the behavior of population balance equations⁴¹⁻⁴³ as well as improvements in rheological constitutive equations for stable suspensions can be systematically and intentionally included in this approach to make improvements in modeling without introducing any new or undefined parameters, as is demonstrated in the following.

Another critically important issue is that of thermodynamic consistency. Larson raised this issue through a simple thought experiment where a structured fluid with infinite viscosity (thixo-elastic material) is deformed in a closed cycle. Such a material, when deformed, will undergo a breakage of internal structure during the deformation, which will then recover when the material is allowed to rest at a fixed strain. During a slow reversal, the stress will be higher than the forward process (because the structure dependent modulus will be higher now that the fluid is fully structured), making the material perform more work on the environment compared to the work required to deform it.¹⁰ The dependence on external kinematics for agglomeration and breakage processes admits such thixo-elastic materials, thus violating the Planck statement of the second law of thermodynamics.²⁵ This imposes a strict restriction on all the phenomenological constants such that they must depend only on the internal variables describing the non-equilibrium state of the liquid (as well as their rates and spatial gradients).^{44,45} Several new models that respect these thermodynamic considerations have been proposed, typically involving a reformulation of the existing phenomenological models in terms of internal variables such as stresses (or conformation tensor) and plastic component of strain rate.^{21,22,25,46} Alternatively, some approaches also derive constitutive models using non-equilibrium thermodynamic formalisms⁴⁷⁻⁴⁹. Using the single-generator bracket formalism of non-equilibrium thermodynamics (SGBF-NET), Jariwala *et al.*⁴⁹ showed that the energy of mixing associated with the particle size distribution is fundamental to generate

aggregation and breakage dynamics required to model thixotropic behavior. The authors also showed that aggregation and breakage depend on the invariants of the internal stresses developed within the agglomerates (modeled via a conformation tensor). Stephanou and Georgiou⁴⁷ were also able to derive a structure kinetics model through the SGBF-NET framework, which they have successfully applied to hemorheology as well.^{48,50}

In this work, we offer an improved, thermodynamically consistent version of the population balance-based approach for rheological constitutive modeling of aggregating suspensions. We show, *without incorporating any additional parameters*, how one can more accurately describes the agglomerate distribution, removing any *a priori* imposition of size distribution to account for polydispersity and its effect on the macroscopic rheological behavior (this model will be hereafter referred to as PBEPoly). We offer a comparison with rheological measurements of suspensions of fumed silica (data from Armstrong *et al.*⁵¹ and Wei *et al.*⁵²) and carbon black dispersion in mineral oil (data from Hipp *et al.*³⁷) for a range of shear rheology protocols (steady shear, step up and step down in shear rate, large amplitude oscillatory shear experiment (LAOS)) and demonstrate the model's accuracy in prediction as well as agreement with direct measurements of changing fluid microstructure under shear using simultaneous rheology and ultra-small angle neutron scattering measurements (Rheo-uSANS).

This article is organized as follows: in the next section (Section 2) we describe the model equations and their parameterization for shear rheology, followed by a comparison of the model fits and predictions against experimental measurements in Section 3. We also offer some recommendations for future work to improve the accuracy and applicability of this modeling framework before concluding our findings in Section 4.

2. Modeling methodology

2.1. Population balance model for structural thixotropy

The modeling approach is based on the population balance framework developed by Mwasame *et al.*^{26,53}. The authors formulated the master equation based on known kernels for Brownian and shear aggregation as well as shear-induced breakage.⁵⁴⁻⁵⁶ The kernels used here are written in terms of the volume of the agglomerate, m . The integro-differential equation quantifying birth and death processes due to aggregation and breakage is as follows:

$$\begin{aligned} \frac{dn(m,t)}{dt} = & \frac{1}{2} \int_0^m [a(m-m', m'; \dot{\gamma}) + c(m-m', m')] n(m-m') n(m') dm' \\ & - \int_0^\infty [a(m', m; \dot{\gamma}) + c(m', m)] n(m) n(m') dm' \\ & + \int_m^\infty b(m'; \dot{\gamma}) P(m | m') n(m') dm' - b(m; \dot{\gamma}) n(m) \end{aligned} \quad , \quad (1)$$

where, the distribution $n(m,t)$ of particles of size m evolves with birth and death events corresponding to aggregation and breakage processes.¹⁶ Because the agglomeration and breakage are assumed to be self-similar, the fractal dimension, d_f , is held fixed to characterize the length scales ($\sim m^{1/d_f}$) in the shear aggregation and the Brownian aggregation kernels,

$$a(m, m'; \dot{\gamma}) \equiv \frac{4}{3} \alpha a_p^3 |\dot{\gamma}| (m^{1/d_f} + m'^{1/d_f})^3, \quad (2)$$

$$c(m, m') \equiv \left(\frac{2k_B T}{3\mu_s \eta_r W} \right) (m^{1/d_f} + m'^{1/d_f}) (m^{-1/d_f} + m'^{-1/d_f}). \quad (3)$$

In the shear aggregation kernel $a(m, m')$, collision frequency is a function of collision cross-section of the aggregating particles $a_p^3 (m^{1/d_f} + m'^{1/d_f})^3$, weighted by α , the collision efficiency. a_p is the radius of the primary particle, and $\dot{\gamma}$ is the applied shear rate. The absolute value of the shear

rate is used to make the expression independent of shearing direction. In the Brownian kernel $c(m, m')$, W is the Fuchs' stability ratio, a function of interaction potential between colliding particles, k_B is the Boltzmann constant, and T is the temperature of the fluid element. μ_s is the suspending medium viscosity, and η_r is the relative suspension viscosity which depends on the volume fraction of particles in the suspension. Following Mwasame *et al.*,²⁶ the medium viscosity term in the original Smoluchowski formulation of the aggregation kernel is replaced by the suspension viscosity to extend the applicability of the expression which was initially derived for dilute suspensions.

Note that the Brownian kernel does not have an equivalent breakage term to establish equilibrium (stationary state) under no-flow conditions. As a result, the population balance equation does not follow detailed balance in the unmodified form, which allows the agglomerates to grow infinitely large with time. To address this unphysical behavior, the empiricism of Mohtaschemi *et al.*⁵⁷ is adopted whereby both shear and Brownian aggregation terms are weighted with a cut-off function $\beta(\phi_a)$. Here, we define this as:

$$\beta(\phi_a) \equiv \left(\frac{\phi_{\max} - \phi_a}{\phi_{\max} - \phi_{pc}} \right)^{\frac{2}{3-d_f}}, \quad (4)$$

which serves to limit the growth of agglomerates when the volume fraction reaches the maximum packing limit, ϕ_{\max} . The maximum packing limit varies with polydispersity.^{58,59} The cut-off function introduced here differs from the one in previous work²⁶, where a hyperbolic tangent function was used. The motion of particles slows down significantly when they are surrounded by a dense network of agglomerates. Eq. (4) captures this effect as the timescale of agglomerate movement

follows the same scaling as the elasticity in the network, albeit in the opposite sense, meaning that as the network becomes more rigid (increase in elasticity), the cut-off function decreases.

Although colloidal agglomerate breakage has been studied extensively at very high shear rates through detailed Stokesian dynamics simulations,^{55,56} breakage at intermediate and low shear rates and the resulting daughter distribution is still an open problem, especially when agglomerates form system spanning networks. For simplicity, we assume the breakage kernel is linear order in agglomerate size and a power-law in shear rate as described by Spicer and Pratsinis⁵⁴,

$$b(m, \dot{\gamma}) = b_0 \dot{\gamma}^2 \left(m^{\frac{1}{d_f}} - m_p^{\frac{1}{d_f}} \right), \quad (5)$$

with a modification to limit the minimum size at m_p . Physically, m_p represents the size of the primary clusters, which are irreversibly linked and cannot be disintegrated through shearing. Apparent volume fraction corresponding to this size is $\phi_{pc} = \phi_p m_p^{3/d_f - 1}$. This lower limit results in the population tending to a monodisperse asymptotic solution at high shear rates.

Shear rate scaling in the breakage expression must correspond to the viscous dissipation due to shear flow, because the agglomerate breakage process must be purely dissipative to be thermodynamically admissible.⁴⁹ This necessitates that the shear rate involved in the breakage kernel be purely plastic or unrecoverable in nature. From a mechanistic standpoint, breakage is caused by the stresses developed within the agglomerate rather than the external kinematics imposed on the material; therefore, it is essential that the structural evolution equations do not depend on total strain rate. This criterion ensures that the resulting equations do not admit thixo-elastic materials which are shown to be non-physical.^{10,25,49} In Maxwell-type viscoelastic constitutive equations for stress, Joshi has proven that thermodynamic consistency can be enforced by decomposing the total

shear strain rate into its elastic and plastic contributions, ensuring that shear aggregation and breakage depend only on the plastic component of the shear strain rate.²⁵ Following this development, one can still use the empirically-constructed breakage kernels and retain their accuracy without violating the thermodynamic admissibility. The strain rate $\dot{\gamma}$ is simply replaced by $\dot{\gamma}_p$ (the viscous part of strain rate) in the shear aggregation, $a(m, m', \dot{\gamma}_p)$ and shear breakage, $b(m, \dot{\gamma}_p)$ kernels ($\dot{\gamma}_p$ is derived in the subsection on *Viscoelasticity*).

The integro-differential form of the population balance equation, Eq. (1), can be converted to a system of ordinary differential equations using the method of moments. This approach generates an infinite set of simultaneous equations that involve fractional moments requiring a closure rule. In this work, we use the Method of Moments with Interpolative Closure (MOMIC) described by Diemer *et al.*^{42,60} This approach approximates the fractional moments of the distribution in terms of the integer moments using a polynomial interpolation (see Appendix B. for details). The key advantage of this approach is that it does not impose the distribution *a priori*; rather, the distribution $n(m, t)$ arises naturally from the choice of kernels, allowing one to describe populations with complexities, such as bimodality, just by solving for additional integer moments. The detailed derivation of the moment equations is presented in Appendix A., and the final expressions are as follows:

$$\begin{aligned}
 0^{\text{th}} \text{ moment: } \frac{d\mu_0}{dt} = & \frac{\phi_p \beta \alpha}{\pi} |\dot{\gamma}| \left(-\mu_{\frac{3}{d_f}} \mu_0 - 3\mu_{\frac{2}{d_f}} \mu_{\frac{1}{d_f}} \right) + \frac{\phi_p kT}{2\pi a_p^3 \mu_s \eta W} \left(-\mu_0^2 - \mu_{\frac{1}{d_f}} \mu_{-\frac{1}{d_f}} \right) \\
 & + b_0 |\dot{\gamma}|^2 (\theta_0 - 1) \left(\mu_{\frac{1}{d_f}} - m_p^{\frac{1}{d_f}} \mu_0 \right), \tag{6}
 \end{aligned}$$

$$1^{\text{st}} \text{ moment: } \frac{d\mu_1}{dt} = 0, \quad (7)$$

$$\begin{aligned} k^{\text{th}} \text{ moment } (k \geq 2): \frac{d\mu_k}{dt} = & \frac{\phi_p \beta \alpha}{2\pi} |\dot{\gamma}| \sum_{n=1}^{k-1} {}^k C_n \left(\mu_{k-n+\frac{3}{d_f}} \mu_n + 3\mu_{k-n+\frac{2}{d_f}} \mu_{n+\frac{1}{d_f}} + 3\mu_{k-n+\frac{1}{d_f}} \mu_{n+\frac{2}{d_f}} \mu_{k-n} \mu_{n+\frac{3}{d_f}} \right) \\ & + \frac{\phi_p \beta k T}{4\pi \alpha_p^3 \mu_s \eta W} \sum_{n=1}^{k-1} {}^k C_n \left(2\mu_{k-n} \mu_n + \mu_{k-n+\frac{1}{d_f}} \mu_{n-\frac{1}{d_f}} + \mu_{k-n-\frac{1}{d_f}} \mu_{n+\frac{1}{d_f}} \right) \\ & + b_0 |\dot{\gamma}|^2 (\theta_k - 1) \left(\mu_{k+\frac{1}{d_f}} - m_p^{\frac{1}{d_f}} \mu_k \right). \end{aligned} \quad (8)$$

The birth due to breakage term in the population balance equation also involves the distribution of daughter fragments, $P(m|m')$. The daughter distribution is modeled using a beta distribution generalized for an arbitrary number of fragments following Diemer and Olson⁴³, whose moments θ_k given by,

$$\theta_k = n_d \frac{\Gamma(s_d + k)}{\Gamma(s_d)} \frac{\Gamma(s_d + s_d(n_d - 1))}{\Gamma(s_d + s_d(n_d - 1) + k)}, \quad (9)$$

where n_d is the number of daughter fragments and s_d is a shape parameter for the distribution. This description can account for more complex mechanisms of breakage, but in this work, we limit our analysis to binary and uniform breakage by setting $n_d = 2$, $s_d = 1$. Because the distribution is written as a function of volume, the first moment is the total solids volume which is conserved. The zeroth moment is related to the average number of primary particles per agglomerate, which makes it a particularly useful descriptor to track as will be shown. The subsequent integer moments can be related to the variance (μ_2), skewness (μ_3), kurtosis (μ_4), and hyp skewness (μ_5) of the agglomerate size distribution using appropriate standardization.

2.2. Yield stress

Yield stress depends on the extent of network formation and hydrodynamic interactions between large and small aggregates. Although the phenomenology of yield stress has been replicated using non-linear viscoelastic constitutive relationships,^{46,49,61} it is difficult to directly associate the parameters with the fractal structure of the agglomerates. Following Shih *et al.*⁶² model for effective elastic modulus G , and elastic strain γ_e , in the strong link regime, the yield stress can be described as

$$\sigma_y(\phi_a) \equiv G(\phi_a)\gamma_e(\phi_a) = \sigma_{y0} \left(\frac{\phi_a - \phi_{pc}}{\phi_{max} - \phi_{pc}} \right)^{\frac{2}{3-d_f}}, \quad (10)$$

where $\sigma_{y0} = G_0\gamma_{e0}$ is the yield stress at equilibrium.

2.3. Kinematic hardening

Kinematic hardening is added explicitly using a back stress to indicate the shift of the yield plane in the direction of deformation (also known as the Bauschinger effect). This modeling approach was proposed by Armstrong and Frederick⁶³ for plastic materials and later extended to elasto-viscoplastic materials by Dimitriou and McKinley⁶⁴. The equation used in this work is due to Wei *et al.*⁶⁵,

$$\frac{dA}{dt} = \dot{\gamma}_p \left(1 - q A \operatorname{sgn}(\dot{\gamma}_p) \right), \quad (11)$$

where q is a fit parameter and A is the back strain that corrects the stress predicted by the constitutive model,

$$\sigma_{eff} = \sigma - k_h \left(\frac{\phi_a - \phi_{pc}}{\phi_{max} - \phi_{pc}} \right)^{\frac{2}{3-d_f}} A, \quad (12)$$

based on the kinematic strain hardening theory. The parameter k_h is the equilibrium back stress modulus such that the back stress expression bears the same structural scaling as the yield stress. In contrast to Wei *et al.*,²¹ here the back stress modulus becomes vanishingly small as the fluid becomes completely unstructured, consistent with the idea that there should not be any elastic effects in the limit of large deformation.

2.4. Viscosity

The viscosity description is usually based on Krieger-Dougherty,⁶⁶ Maron-Pierce,⁶⁷ or Quemada-type relationship,^{68,69} where the viscosity diverges as the volume fraction of agglomerates approaches the random close packing limit. Here we use a Krieger-Dougherty model:

$$\mu = \mu_s \left(1 - \frac{\phi_h}{\phi_{max}} \right)^{-2.5\phi_{max}}. \quad (13)$$

For a polydisperse system, the relative viscosity expression requires correction to include the effects due to smaller particles. The presence of smaller particles has a two-fold contribution to the overall viscosity; first, an increase in the background viscosity because the smaller particles act as an effective medium in which the larger particles are suspended. Secondly, they also occupy an effective volume in the suspending medium. Without including these contributions, one would underpredict the overall viscosity for the same volume fraction. Polydisperse particles can also pack much closer compared to the random close packing limit for monodisperse hard spheres ($\phi_{max}^{mono} \sim 0.64$). The maximum packing limit for a lognormally-distributed population of hard sphere has been obtained by Farr and Groot⁵⁹ where the authors generated three-dimensional random

close packing of spheres via simulation and mapped it onto a distribution of one-dimensional rods. The simulation data for the maximum packing limit has been fit to an analytic expression by Farr,⁵⁸

$$\sigma_p = \sqrt{\ln\left(\frac{\mu_{4/d_f} \mu_{2/d_f}}{\mu_{3/d_f}^2}\right)},$$

$$\phi_{\max,rcp}^{\text{poly}}(\sigma_p) = 1 - 0.57e^{-\sigma_p} + 0.2135e^{-0.57\sigma_p/0.2135} + 0.0019\left\{\cos\left[2\pi\left(1 - e^{-0.75\sigma_p^{0.7} - 0.025\sigma_p^4}\right)\right] - 1\right\}, \quad (14)$$

which agrees with the results up to four decimal places. The viscosity expression for polydisperse non-colloidal suspensions derived by Mwasame *et al.*³⁸⁻⁴⁰ uses the size distribution of the agglomerates in the form of abscissa (m_i) and weights (ω_i) of the quadrature,

$$\mu_k = \sum_{i=1}^N \omega_i m_i^k. \quad (15)$$

This inverse problem calculation is performed using the product-difference algorithm proposed by Gordon⁷⁰ and McGraw.⁷¹ Using the first 6 moments of the size distribution ($k = 0, 1, \dots, 5$), a ternary population can be described such that the volume fractions of each component is given as

$$\phi_{D_1} = \frac{\omega_1}{\sum_{i=1}^3 \omega_i} \phi_a, \quad \phi_{D_2} = \frac{\omega_2}{\sum_{i=1}^3 \omega_i} \phi_a, \quad \phi_{D_3} = \frac{\omega_3}{\sum_{i=1}^3 \omega_i} \phi_a, \quad (16)$$

where ϕ_{D_i} are the volume fractions corresponding to each abscissa, and the respective sizes, D_i are given as $D_i = K m_i^{1/d_f}$. Because this calculation only involves the ratios of diameters, the pre-factor K can be neglected. The relative viscosity is then determined using the hydrodynamic function

$$\eta_r(\mu_k) \equiv \exp(f_{tri}(\mu_k)). \quad (17)$$

The complete definition of $f_{tri}(\mu_k)$ is provided in the Appendix C. Assuming self-similarity, a correction to account for the effective hydrodynamic volume fraction ϕ_{h,D_i} can be included as,

$$\phi_{h,D_i} = \left(\frac{R_h}{R_a}\right)^3 \phi_{D_i}, \quad (18)$$

with R_h/R_a being the ratio of hydrodynamic radius to the radius of the aggregate. For this work, the ratio R_h/R_a is held constant for all volume fractions ϕ_{D_i} .

2.5. Viscoelasticity

Viscoelasticity is modeled using a constitutive relationship based on work by Kamani *et al.*⁷² where the authors propose a phenomenological equation for modeling yield-stress fluids, given as

$$\sigma + \tau(\dot{\gamma}) \frac{d\sigma}{dt} = \left(\frac{\sigma_y}{|\dot{\gamma}|} + K |\dot{\gamma}|^{n-1} \right) (\dot{\gamma} + \tau' \ddot{\gamma}). \quad (19)$$

At steady state, the proposed equation reduces to the Herschel-Bulkley model for yield-stress materials. The authors unify the physics of pre-yield and post-yield state of the material by removing the discontinuity in the Oldroyd-Prager formalism⁷³⁻⁷⁵ through the use of a rate-dependent relaxation time $\tau(\dot{\gamma})$. The yield stress term behaves like a constant viscous term bearing the same sign as the shear rate and in the absence of explicit solvent contribution, the retardation time τ' vanishes. This is consistent with Jariwala *et al.* TEVP constitutive model derived from non-equilibrium thermodynamics, where the authors have shown that the phenomenology of fluid yield stress can be replicated through non-linear terms in the viscoelasticity expression.⁴⁹ An alternative

expression for this constitutive relation is one proposed by Saramito²³ where an explicit distinction between the elastic and visco-plastic behavior is maintained through the use of a discontinuity,

$$\max\left(0, \frac{|\sigma| - \sigma_y}{|\sigma|}\right) \sigma + \tau \frac{d\sigma}{dt} = \eta \dot{\gamma}. \quad (20)$$

However, we found that the use of such discontinuous functions is hard to justify from a non-equilibrium thermodynamics standpoint as they do not arise naturally from the free energy functionals based on internal structural variables.

A key difference in the use of the constitutive relation Eq. (19) when applied in our work is the structural dependence of the relaxation time instead of the shear rate dependence used by Kamani *et al.*⁷² This is done to guarantee thermodynamic admissibility of the resulting governing equations as the phenomenological quantities must depend on the internal structural variables rather than external kinematics, as shown by Souvaliotis and Beris.⁴⁴ In order to introduce a structural dependence on the relaxation time and elasticity, two modifications are made; (a) a White-Metzner type relaxation time and (b) yield stress that follows the work of Shih *et al.*^{62,76,77} to introduce a scaling with the agglomerate volume fraction. The relaxation time expression is obtained using the zeroth-order characteristic time from the population balance equation, following the previous work,²⁶ such that

$$\tau(\mu_k) = \frac{1}{\dot{\gamma}_{ss}(\mu_k)} \frac{\sigma_{y0}}{G_0} \left| \frac{\sigma_{y0}}{\sigma_y} \right|^p. \quad (21)$$

Here, p is a White-Metzner power-law parameter. The characteristic structural shear rate, $\dot{\gamma}_{SS}(\mu_k)$, is defined through the stationary point of the zeroth moment evolution equation such that

$$\left. \frac{d\mu_0}{dt} \right|_{\dot{\gamma}=\dot{\gamma}_{SS}} = 0, \text{ i.e.,}$$

$$\dot{\gamma}_{SS}(\mu_k) = \frac{-B + \sqrt{(B^2 + 4AC)}}{2A} \text{ with}$$

$$A = b_0(\theta_0 - 1) \left(\mu_{\frac{1}{d_f}} - m_{\frac{1}{d_f}} \mu_0 \right)$$

$$B = \frac{\phi_p \beta \alpha}{\pi} \left(-\mu_{\frac{3}{d_f}} \mu_0 - 3\mu_{\frac{2}{d_f}} \mu_{\frac{1}{d_f}} \right)$$

$$C = \frac{\phi_p kT}{2\pi \alpha_p^3 \mu_s \eta W} \left(-\mu_0^2 - \mu_{\frac{1}{d_f}} \mu_{\frac{1}{d_f}} \right).$$
(22)

The separation of time scales is ensured in this framework by using two distinct timescales for thixotropy and viscoelasticity: one emerging from aggregation and breakage rates, and the other corresponding to deformation rates and strains. In order to include kinematic hardening, the stress term in the viscoelastic constitutive equation is replaced with σ_{eff} as calculated in Eq. (12). The final stress constitutive equation then becomes,

$$\sigma_{eff} + \tau(\mu_k) \frac{d\sigma}{dt} = \left(\frac{\sigma_y(\phi_a)}{\dot{\gamma}_{SS}(\mu_k)} + \mu_s \eta_r(\mu_k) \right) \dot{\gamma}. \quad (23)$$

This equation can also be re-written as

$$\dot{\gamma} = \dot{\gamma}_e + \dot{\gamma}_p = \frac{\tau(\mu_k)}{\left(\frac{\sigma_y(\phi_a)}{\dot{\gamma}_{SS}(\mu_k)} + \mu_s \eta_r(\mu_k) \right)} \frac{d\sigma}{dt} + \frac{\sigma_{eff}}{\left(\frac{\sigma_y(\phi_a)}{\dot{\gamma}_{SS}(\mu_k)} + \mu_s \eta_r(\mu_k) \right)}, \quad (24)$$

decomposing the total shear strain rate as a sum of its elastic and plastic parts (or recoverable and unrecoverable parts). Following this idea, the plastic component of shear rate is described as,

$$\dot{\gamma}_p = \frac{\sigma_{eff}}{\frac{\sigma_y(\phi_a)}{\dot{\gamma}_{SS}(\mu_k)} + \mu_s \eta_r(\mu_k)}. \quad (25)$$

The plastic component of shear rate is now completely determined by stress and structural state of the systems, making it fully consistent with thermodynamics and the mechanistic picture of agglomerate breakage. At steady state, the plastic component of shear strain is identical to the total strain rate, i.e., $\dot{\gamma}_p(t \rightarrow \infty) = \dot{\gamma}$. The stress constitutive relation at steady state reduces to,

$$\sigma_{SS} = \left(\sigma_{y_0} + \frac{k_h}{q} \right) \left(\frac{\phi_a - \phi_{pc}}{\phi_{max} - \phi_{pc}} \right)^{\frac{2}{3-d_f}} \text{sgn}(\dot{\gamma}) + \mu_s \eta_r(\mu_k) \dot{\gamma}. \quad (26)$$

3. Results and Discussion

3.1. Model parameters and their estimation

The model consists of a system of simultaneous ordinary differential equations,

$\left[\frac{d\mu_k}{dt}, \frac{d\sigma}{dt}, \frac{dA}{dt} \right]^T$. The equations describe the time evolution of the integer moments of ag-

glomerate size distribution μ_k , the overall stress σ , and the back strain A . Only the first six

scaled integer moments are included in the solution ($\mu_k, k = 0, 1, 2, 3, 4, 5$). As the first moment μ_1

is fixed because of mass conservation requirements $\left(\frac{d\mu_1}{dt} = 0 \right)$, only five moment equations

need to be solved. The model equations are summarized in TABLE 1. The model involves a total

of fifteen parameters $\left(a_p, \phi_p, \phi_{max}^{mono}, \sigma_{y_0}, k_h, q, T, W, \alpha, b_0, d_f, \frac{R_h}{R_a}, m_p, G_0, p \right)$, however four of

these, $a_p, \phi_p, \phi_{\max}^{\text{mono}}, T$ can be readily determined from the sample preparation parameters, heuristics, and experimental conditions. The remaining eleven are estimated here by fitting the model to steady state and transient rheological experimental data, although we note that some of these can be estimated or independently determined by supplementary measurements. Note that the fit parameters may not be completely independent. In some instances, the morphological parameters in aggregating suspensions can be determined from theory, simulations, and experiment. For example, the Kirkwood-Riseman theory relates the fractal dimension to the porosity and the hydrodynamic radius of the agglomerate but its applicability is limited to spherically symmetric open/porous aggregates.⁷⁸

A parallel tempering optimization algorithm by Armstrong *et al.*,⁷⁹ which is efficient in determining the fit parameters for highly non-linear models, is used to determine these fit parameters. This fitting approach overcomes the computational penalty of starting from a poor initial guess by utilizing parallel runs to avoid local trapping. A cost function must be defined first to use this fitting procedure that appropriately weights the experiments. Following the work by Armstrong *et al.*,⁸⁰ we use two cost functions, $F_{\text{obj,SS}}$ and $F_{\text{obj,tran}}$ for steady state and transient experiments, which are defined as,

$$\begin{aligned}
 F_{\text{obj,SS}} &= \frac{1}{M_{\text{SS}}} \sum_{k=1}^{M_{\text{SS}}} \left\| \frac{\sigma_{\text{model},k} - \sigma_{\text{data},k}}{\sigma_{\text{data},k}} \right\|_2, \\
 F_{\text{obj,tran}} &= \frac{1}{M_{\text{tran}}} \sum_{k=1}^{M_{\text{tran}}} \frac{1}{P_k} \left\| \frac{\sigma_{\text{model},k} - \sigma_{\text{data},k}}{\bar{\sigma}_{\text{data},k}} \right\|_2,
 \end{aligned} \tag{27}$$

where P_k are the number of points in a transient experiment, and M_{SS} and M_{tran} are the number of steady state and transient experiments, respectively. The parallel tempering algorithm takes the initial guess values of the parameters, some of which are bounded, and minimizes the cost function

$F_{\text{obj}} = F_{\text{obj,SS}} + F_{\text{obj,tran}}$ to return the optimal values of the parameters. Both steady state and transient data are needed as the governing equations admit multiple solutions for the parameters due to nonlinearities. Appropriate bounds are chosen such that the parameter values agree with physical intuition. Set of parameters that gives the minimum value for the cost function is chosen as the best fit.

The datasets of experiments used for fitting and comparison includes fumed silica suspensions by Armstrong *et al.*⁷⁹ and Wei *et al.*,⁵² both consisting of 2.9 vol.% Evonic Aerosil R972 particles (~16 nm) suspended in 69 wt% paraffin oil and 31 wt% polyisobutylene. The compositions of the suspending medium and primary particles used for these two suspensions appear to be very similar; however, data by Wei *et al.*⁵² were obtained after 20 days of sample preparation. This was done to have repeatability in measurements. We suspect that this delay in measurement caused quiescent restructuring at the primary cluster level, which in turn caused the rheological behavior of these two samples to be distinct.

Because we are also comparing the model (PBEPoly) against previous iterations of the population balance model (PBEMono) and the multi-lambda structure kinetics model by Wei *et al.* (ML-IKH), we have used a similar set of experimental data for fitting. This includes the steady state flow curve along with a set of step shear experiments to represent the transient data. The intermediate shear rate regime has the most prominent thixotropic response, and thus requires more transient experiments to be resolved. For the fumed silica dataset of Armstrong *et al.*⁷⁹, in addition to the steady state flow curves, we have used nine step shear experiments: four step downs [5 s^{-1} to $2.5, 1.0, 0.5, 0.1 \text{ s}^{-1}$] and five step ups [0.1 s^{-1} to $5, 2.5, 1.0, 0.5, 0.25 \text{ s}^{-1}$]. For Wei *et al.* data, only

three step-up experiments in shear rate were used for transients [0.1 s^{-1} to $5, 2.5, 1.0 \text{ s}^{-1}$] (similar to what the authors have used for their ML-IKH model²¹).

An additional comparison is made for the dataset of a carbon black dispersion (4.95 wt% Vulcan XC-72 (~20 nm primary particles) in mineral oil) from Hipp *et al.*,³⁷ for which, in addition to the rheological measurements, the authors also conducted simultaneous rheological and ultra-small angle neutron scattering measurements (Rheo-uSANS). This enables us to directly compare the structure predictions made by PBEPoly with the radius of gyration estimated from scattering intensity profiles. A limitation with this formulation of carbon black dispersion is that whenever the stress drops below the yield stress, the suspension undergoes irreversible structural transition and loses the reversible thixotropic characteristics.³⁷ In some formulations, carbon black suspensions also exhibit antithixotropy or rheopexy which has been hypothesized to arise due to formation vorticity aligned structures during long transients at low-intermediate shear rate regime.^{81,82} Because a scalar description is used to describe mesoscale structure in our modeling, predicting alignment and spatial heterogeneities would require invoking additional structural descriptors. So, for this dataset, the fitting procedure only included the steady state data at higher shear rates, such that $\sigma > \sigma_y$, along with four step-downs in shear rate [2500 s^{-1} to $1000, 500, 100, 50 \text{ s}^{-1}$].

The parameters generated from the fitting are tabulated in TABLE 2. The fit parameter values agree favorably with the physical intuition, especially the fractal dimension which agrees with the reaction limited aggregation and is in the range 2.1-2.5.³⁴ The fractal dimension for the carbon black dispersion was estimated to be $d_f^{\text{Rheo-uSANS}} = 2.53 \pm 0.025$ from scattering measurements, which is quite close to the one determined from fitting $d_f^{\text{PBEPoly}} = 2.37 \pm 0.01$ (the error bounds are standard deviations determined from 15 independent runs). Note that the fractal dimension in this

approach is a fixed parameter such that any agglomerate restructuring or compaction that might change the fractal dimension is neglected.

TABLE 1. Summary of the equations used for the model presented in the paper (PBEPoly) and ML-IKH²¹ model in this article.

	PBEPoly	ML-IKH ²¹ (rate-controlled form)
Parameters	15 total, 11 fit parameters $(a_p, \phi_p, \phi_{\max}^{\text{mono}}, \sigma_{y0}, k_h, q, T, W, \alpha, b_0, d_f, R_h/R_a, m_p, G_0, p)$	12 fit parameters $(k_y, k_h, q, G, \eta_{thi}, \eta_m, \beta, a, n, k_1, k_2, k_3)$
Structure evolution	Population balance equation using MOMIC (Method Of Moments with Interpolative Closure) $\frac{d\mu_0}{dt} = \frac{\phi_p \beta \alpha}{\pi} \dot{\gamma}_p \left(-\mu_{\frac{3}{d_f}} \mu_0 - 3\mu_{\frac{2}{d_f}} \mu_{\frac{1}{d_f}} \right)$ $+ \frac{\phi_p kT}{2\pi a_p^3 \mu_s \eta W} \left(-\mu_0^2 - \mu_{\frac{1}{d_f}} \mu_{\frac{1}{d_f}} \right)$ $+ b_0 \dot{\gamma}_p ^2 (\theta_0 - 1) \left(\mu_{\frac{1}{d_f}} - m_p^{\frac{1}{d_f}} \mu_0 \right),$ $\frac{d\mu_k}{dt} = \frac{\phi_p \beta \alpha}{2\pi} \dot{\gamma}_p \sum_{n=1}^{k-1} {}^k C_n \left(\begin{aligned} &\mu_{k-n+\frac{3}{d_f}} \mu_n + 3\mu_{k-n+\frac{2}{d_f}} \mu_{n+\frac{1}{d_f}} \\ &+ 3\mu_{k-n+\frac{1}{d_f}} \mu_{n+\frac{2}{d_f}} \mu_{k-n} \mu_{n+\frac{3}{d_f}} \end{aligned} \right)$ $+ \frac{\phi_p \beta kT}{4\pi a_p^3 \mu_s \eta W} \sum_{n=1}^{k-1} {}^k C_n \left(\begin{aligned} &\mu_{k-n+\frac{1}{d_f}} \mu_{n-\frac{1}{d_f}} + 2\mu_{k-n} \mu_n \\ &+ \mu_{k-n-\frac{1}{d_f}} \mu_{n+\frac{1}{d_f}} \end{aligned} \right)$ $+ b_0 \dot{\gamma}_p ^2 (\theta_k - 1) \left(\mu_{k+\frac{1}{d_f}} - m_p^{\frac{1}{d_f}} \mu_k \right),$ <p>$k = 2, 3, 4, 5.$</p>	Structure kinetics model with stretched exponential structure relaxation $\frac{d\lambda_i}{dt} = D_i \left[(k_3 + k_2 \dot{\gamma}_p ^{0.5}) (1 - \lambda_i) - k_1 \lambda_i^n \dot{\gamma}_p ^a \right],$ $\lambda = \sum_{i=1}^N C_i \lambda_i,$ $\exp(-t^\beta) = \sum_{i=1}^N C_i (\beta) e^{-D_i t}.$
Viscosity	Suspension viscosity expression $\mu_s \eta_r$ $\eta_r(\mu_k) \equiv \exp(f_{tri}(\mu_k))$	Structural + Solvent viscosity $\lambda \eta_{thi} + \eta_m$
Yield Stress	$\sigma_{y0} \left(\frac{\phi_a - \phi_{pc}}{\phi_{\max} - \phi_{pc}} \right)^{\frac{2}{3-d_f}}$	λk_y
Plastic strain rate	$ \dot{\gamma}_p = \frac{ \sigma_{eff} }{\frac{\sigma_y(\phi_a)}{\dot{\gamma}_{SS}(\mu_k)} + \mu_s \eta_r(\mu_k)}$	$ \dot{\gamma}_p = \begin{cases} 0 & \sigma_{eff} < \lambda k_y \\ \frac{ \sigma_{eff} - \lambda k_y}{\lambda \eta_{thi}} & \sigma_{eff} \geq \lambda k_y \end{cases}$

Back strain	$\frac{dA}{dt} = \dot{\gamma}_p (1 - qA \operatorname{sgn}(\dot{\gamma}_p))$	$\frac{dA}{dt} = \dot{\gamma}_p (1 - qA \operatorname{sgn}(\dot{\gamma}_p))$
Stress constitutive relation	$\sigma_{eff} + \tau(\mu_k) \frac{d\sigma}{dt} = \left(\frac{\sigma_y(\phi_a)}{\dot{\gamma}_{SS}(\mu_k)} + \mu_s \eta_r(\mu_k) \right) \dot{\gamma}$	$\max \left(0, \frac{ \sigma_{eff} - \lambda k_y}{ \sigma_{eff} } \right) \sigma_{eff} + \lambda \theta \frac{d\sigma}{dt} = \lambda \eta_{thi} \dot{\gamma}$
Steady state	$\sigma_{SS} = \left(\sigma_{y0} + \frac{k_h}{q} \right) \left(\frac{\phi_a - \phi_{pc}}{\phi_{max} - \phi_{pc}} \right)^{\frac{2}{3-d_f}} \operatorname{sgn}(\dot{\gamma}) + \mu_s \eta_r(\mu_k) \dot{\gamma}$	$\sigma_{SS} = \left(\lambda_{SS} k_y + \frac{k_h}{q} \right) \operatorname{sgn}(\dot{\gamma}) + (\eta_m + \lambda_{SS} \eta_{thi}) \dot{\gamma}$

TABLE 2. Model parameters and objective functions for the three datasets under consideration. The unshaded parameter values for each set are predetermined from the sample preparation and specific aspects of the data. The fit (shaded) parameter values were obtained after 15 independently initialized runs of parallel tempering algorithm.⁷⁹ The complete set of parameters obtained from the runs are provided in Tables S1-3.

	Suspensions		
	Carbon black (Hipp <i>et al.</i> ³⁷)	Fumed silica (Armstrong <i>et al.</i> ⁵¹)	Fumed silica (Wei <i>et al.</i> ⁵²)
a_p	10 nm	8 nm	8 nm
ϕ_{max}^{mono}	0.64	0.64	0.64
T	298 K	298 K	298 K
q	1	1	1
p	3	3	3
ϕ_p	0.028	0.03	0.03
σ_{y0}	10.42 ± 0.11 Pa	2.43 ± 0.15 Pa	0.59 ± 0.02 Pa
k_h	0 Pa	8.6 ± 0.4 Pa	0.30 ± 0.01 Pa
W	5.32 × 10 ⁻³ ± 4 × 10 ⁻⁵	0.0091 ± 0.0003	19.68 ± 1.85
α	0.97 ± 0.01	0.76 ± 0.06	0.64 ± 0.02
b_0	4.54 × 10 ⁻⁵ ± 4.1 × 10 ⁻⁶ s	7.6 × 10 ⁻³ ± 2.1 × 10 ⁻³ s	2.21 × 10 ⁻³ ± 2.5 × 10 ⁻⁴ s
d_f	2.37 ± 0.01	2.05 ± 0.12	2.29 ± 0.02
R_h/R_a	0.988 ± 0.002	0.939 ± 0.008	0.85 ± 0.01
m_p	316 ± 14	220 ± 38	475 ± 74
G_0	1070 ± 10 Pa	808 ± 47 Pa	37.5 ± 0.8 Pa
μ_s	0.0224 ± 0.0002 Pa s	0.41 Pa s †	0.367 ± 0.008 Pa s
		† Determined from independent measurement	
$F_{obj,SS}$	0.01154	0.01375	0.00697
$F_{obj,trans}$	0.35316	0.59145	0.33282

3.2. Steady shear

The steady state equations are solved by setting the time derivatives $d\mu_k/dt$, $d\sigma/dt$ and dA/dt to 0 and solving the corresponding non-linear equations for a range of shear rates. Compared to the monodisperse version of the constitutive model (PBEMono), the new model (PBEPoly) provides more accurate steady state fits that are comparable to ML-IKH (see Figure 1 (a)). The main advantage of the population balance approach for modeling the structural evolutions is the insight it provides into the mesoscale structure through the agglomerate size distribution and quantities such as mass mean radius and apparent volume fraction swept by the agglomerate structures. Consistent with the argument $\phi_{\max}^{\text{mono}} < \phi_{\max}^{\text{poly}}$, we see in Figure 1 (b) that the predicted volume fraction at lower shear rates from the PBEPoly model are higher than PBEMono. The volume fraction shows similar trends with shear rate, i.e., decreasing in value because of agglomerate breakage. The moments of the size distribution vary independently, yet at higher shear rates, the magnitude of all integer moments μ_k , $k \geq 2$ starts decreasing with shear rate indicating that the distribution is narrowing (Figure 1 (c)). This is because the agglomerate size is approaching the minimum size limit set by $m_{\min} = m_p$ in the breakage kernel. This limit forces the distribution to tend to monodisperse distribution because the primary clusters are assumed to be monodisperse. Although we found this assumption to hold quite well for the rheological protocols examined in this work, it has been observed that the primary particle and primary cluster size distribution may have some polydispersity.^{82,83} This polydispersity may become critical when the high-shear rheology of aggregated particles is being examined. This assumption can be relaxed, though determining the primary particle/cluster distribution will introduce additional fit parameters.

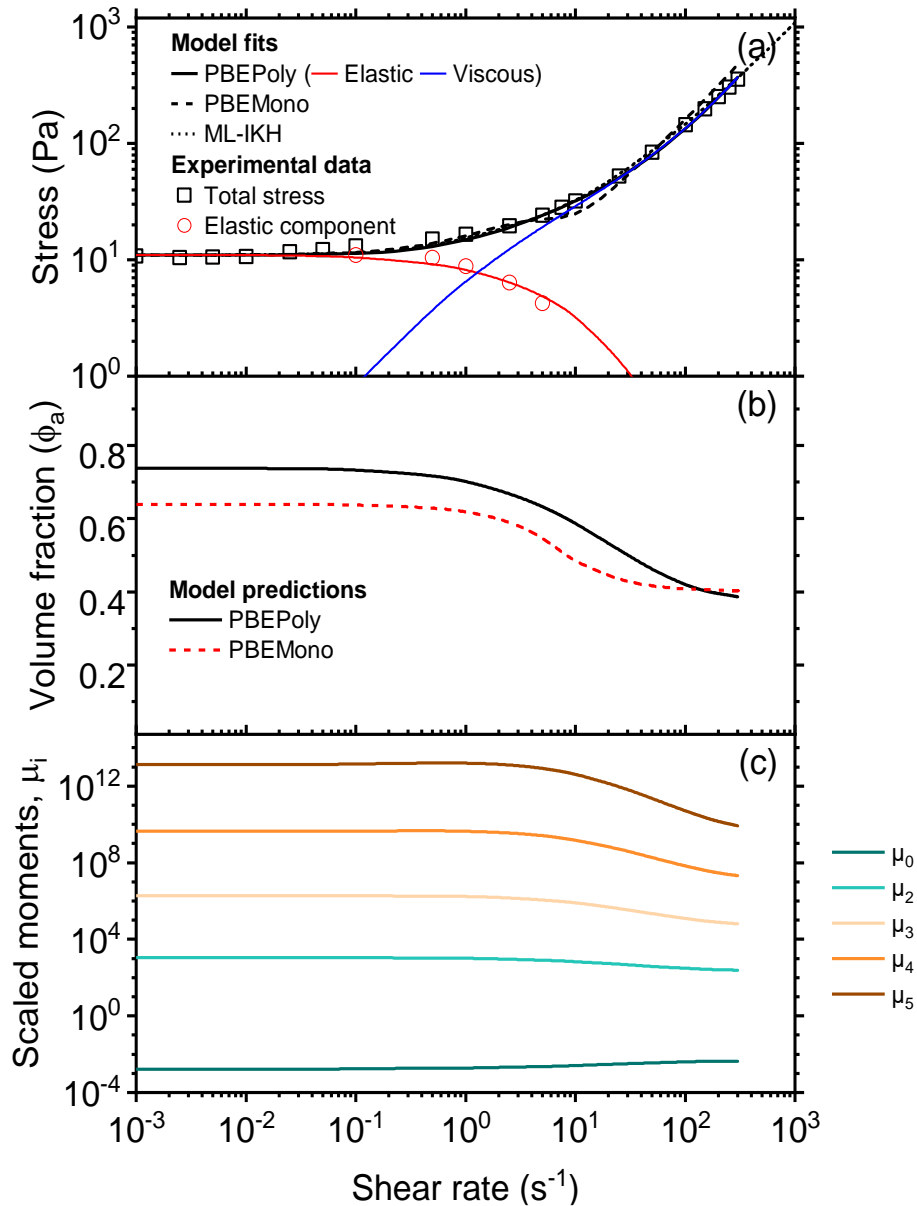


Figure 1 (a) Steady state flow curve for the fumed silica suspension (data from Armstrong *et al.*⁵¹) indicating the shear stress as a function of shear rate. The lines indicate the PBEPoly (solid), PBEMono (dashed), ML-IKH (dotted) model fits to the experimental data denoted by square symbols. Note the presence of yield stress (y-axis intercept) because of agglomerate networks at lower shear rates. The predictions of elastic and viscous components of stress for PBEPoly model are plotted as solid red and blue lines, respectively. (b) The volume fraction of agglomerates decreases with increasing shear rates as the networks and bonds between the agglomerates disintegrate. PBEPoly model predicts significantly higher agglomerate volume fraction compared to PBEMono. (c) The scaled moments μ_i as a function of shear rate.

In Figure 2 (a), the steady state flow curve fit from the model is presented along with the computed values of mass mean radius,

$$R_a = K_R \mu_{1+1/d_f}, \quad (28)$$

where, R_a is the mass mean radius and K_R is a pre-factor weighting the μ_{1+1/d_f} moment. The pre-factor depends on the primary particle size and the measurement technique used to determine the agglomerate sizes.⁸⁴ By normalizing the predictions and experimental estimates by their respective minimum values, the pre-factor is canceled out and the scaling behavior with shear rate can be examined. As the behavior at high shear rates is pre-dominantly viscous shear-thinning (thixoviscous in transients), it can be seen that in order to generate similar viscosities, the monodisperse agglomerates need to be much larger in size. The scaling predictions from PBEPoly shown in Figure 2 (b), though not exact, still quite closely agree with experimental estimates. The size estimates from Rheo-uSANS are biased towards larger agglomerate sizes because the form factor is weighted by the square of the agglomerate volume, favoring the larger tail end of the distribution.³⁷ The reconstructed distributions for the carbon black dispersion for a range of shear rates (shown in Figure 3) indicate that the distribution becomes narrower at larger shear rates and the mean agglomerate size decreases, yet the distribution is sufficiently wide to not admit a monodisperse description.

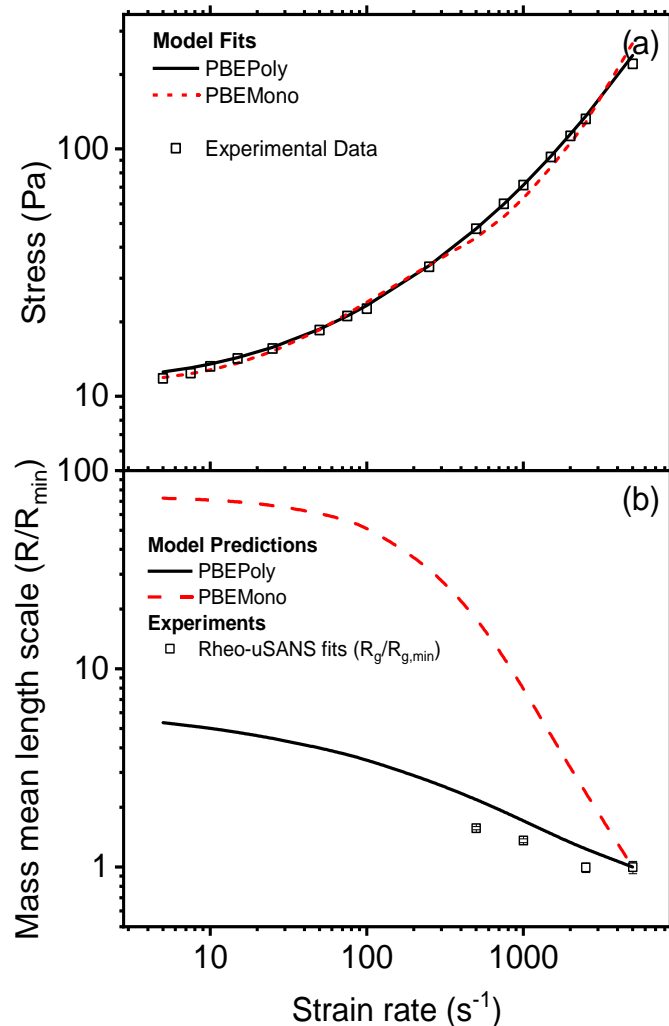


Figure 2 (a) Steady state flow curve model fits using PBEMono and PBEPoly. PBEPoly offers significantly improved steady state fits owing to the polydisperse description of viscosity and elastic modulus. (b) Mass mean length scale prediction of both PBEMono and PBEPoly is compared. The values are normalized by the minimum predicted/measured value in each data set, R_{min} , to get rid of the pre-factor that weights the fractal scaling for estimating radii. The measurements of Rheo-uSANS³⁷ are represented using symbols (the error bars are smaller than the symbols)

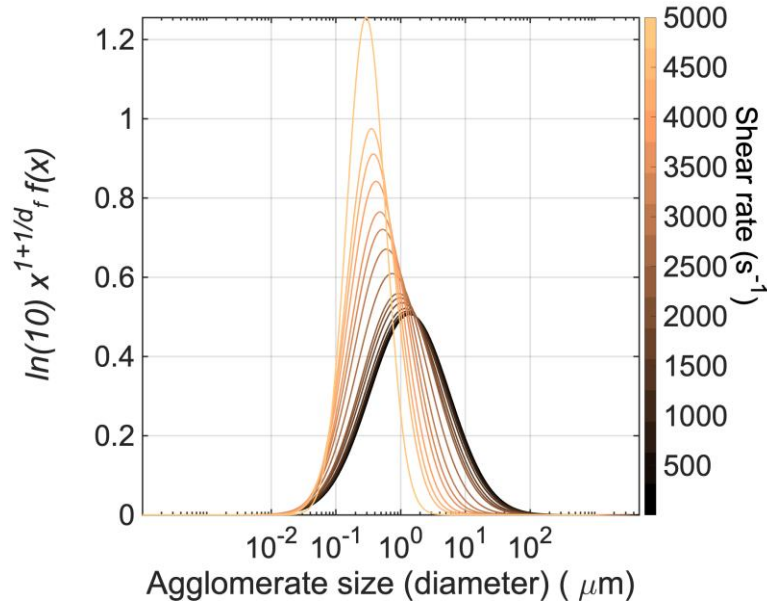


Figure 3. Reconstructed distributions for a range of shear rates calculated using the scaled integer moments $\mu_k, k = 0, 2, 3, 4, 5$ at steady state for Vulcan XC-72 carbon black dispersion based on model fits to Hipp *et al.* data.³⁷ A lognormal distribution reconstruction procedure was used (Appendix D).

3.3. Transients

The transient rheology is described by solving the governing equations (system of ordinary differential equations) in tandem with the coupled relations to determine the rheological properties (as shown in **TABLE 1**). For simple shear flow, the equations can be solved by supplying the shear rate as a function of time for various rheological experiments and generating a time dependent solution using the method of lines. The shear rate step-up and step-down experiments, where the shear deformation rate is suddenly changed, are described by the step function,

$$\dot{\gamma}(t) = \begin{cases} \dot{\gamma}_{initial} & t \leq 0 \\ \dot{\gamma}_{final} & t > 0 \end{cases} \quad (29)$$

The model fits to step shear experiments for fumed silica suspension from Armstrong *et al.*⁵¹ and Wei *et al.*⁵² are shown in Figure 4 (a) and (c), respectively. PBEPoly is able to capture the trends

due to the viscoelastic and thixotropic transient timescales; however, for the step down experiments to low shear rates (for instance from 5 s^{-1} to 0.1 s^{-1} in Figure 4 (a)), there is a systematic discrepancy between model fits and experimental data at short times. This can be attributed directly to the viscoelastic constitutive relation used in this work, Eq. (23). The viscous term $\frac{\sigma_y}{\dot{\gamma}_{ss}} \dot{\gamma}$ does not decrease to a sufficiently low value to allow the stress to undergo a complete viscoelastic relaxation as observed in the experiment.

The apparent volume fraction increases in the case of a step-down experiment because of the decrease in the applied deformation rate. The predicted ϕ_a values in Figure 4 (b) are very close to the random close packing limit, indicating that around these shear rates, it is likely that the agglomerates will begin forming system spanning networks. The viscoelasticity of flocculated networks is still an open problem and their viscoelastic characterization is a subject of ongoing work.⁸⁵ Fractional Kelvin-Voigt models that mimic the limiting behavior of hierarchical networks have been used with some success though the numerics of such a description are quite limiting when it comes to flow modeling applications. The viscoelastic description used in this work is prone to provide poor predictions at lower deformation rates, and the suspected reason is the formation of flocculated system spanning networks that are found in that flow regime.

The model fits shown in Figure 4 are comparable to those for the ML-IKH model for the step transients. PBEPoly captures the thixotropic structural relaxation, and the model can replicate the features of the stretched exponential relaxation distribution that was introduced artificially in the ML-IKH model.

For large amplitude oscillatory shear (LAOS) measurements, the strain and shear rate can be described using the following relations,

$$\begin{aligned}\gamma(t) &= \gamma_0 \sin \omega t, \\ \dot{\gamma}(t) &= \gamma_0 \omega \cos \omega t,\end{aligned}\tag{30}$$

where γ_0 is the strain amplitude and ω is the oscillation frequency of torque applied by the rheometer. LAOS experiments have been shown to capture complex viscoelastic and yielding behaviors and encode the timescales corresponding to thixotropy, viscoelasticity as well as rheological features such as dynamic yield stress.⁸⁶⁻⁸⁹ LAOS experiments capture the directional deformation and the resulting kinematic hardening which are not seen in the steady shear and step transient experiments due to their unidirectional nature. As shown in Figure 5 (a-d), PBEPoly does an adequate job of capturing the sharp viscoelastic and dynamic yield transitions at moderate and high shear rates in LAOS experiments; however, at low strain amplitudes and frequencies, the predictions do not match very well with the experiments. This is a result of the specific choice of viscoelastic constitutive equation, which on the one hand guarantees thermodynamic consistency, but at the same time performs inadequately at low shear rates. This is a clear indication of missing physics that the structurally based relaxation time expressions fail to account for. It may be possible to construct a relaxation time that involves the rates of the agglomerate moment evolution, as shown by Armstrong *et al.*⁹⁰ in their recent work on hemorrheology; however, for the sake of simplicity and not introducing additional parameters, we left this avenue largely unexplored in this work. As discussed earlier, without a clear parallel development in experimental (*in vitro* or *in silico*) observation of strains and evolving structure at mesoscale, one must contend with phenomenology when constructing the stress constitutive relationship. This is further exacerbated in the flow reversal experiments, where the shear rate switches direction in a step change yet retains the

same magnitude. PBEPoly predictions are seen in Figure 6, compared against the data and ML-IKH model, and it is clear that there is a missing piece in the viscoelastic constitutive equation plaguing this formulation. Nonetheless, PBEPoly qualitatively captures the two-step relaxation during flow reversal at lower shear rates.

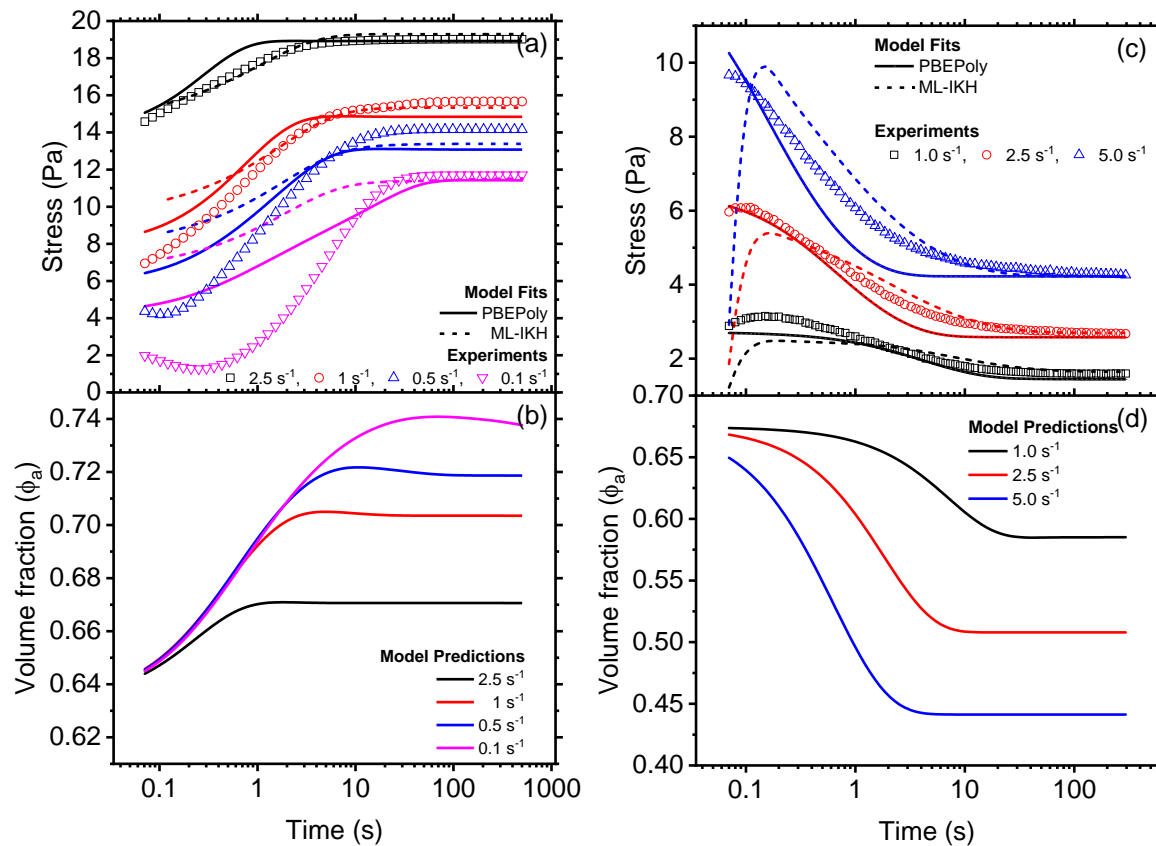


Figure 4 (a) Fits for step down in shear rate from 5 s^{-1} to the indicated values. Both PBEPoly (solid line) and ML-IKH models (dotted line) are compared against the experimental data from Armstrong *et al.*⁵¹ (symbols). (b) PBEPoly predictions for corresponding evolution of apparent volume fraction of the agglomerates. (c) Model fits for step up in shear rate from 0.1 s^{-1} to the indicated value and (d) the corresponding change in the agglomerate volume fraction.

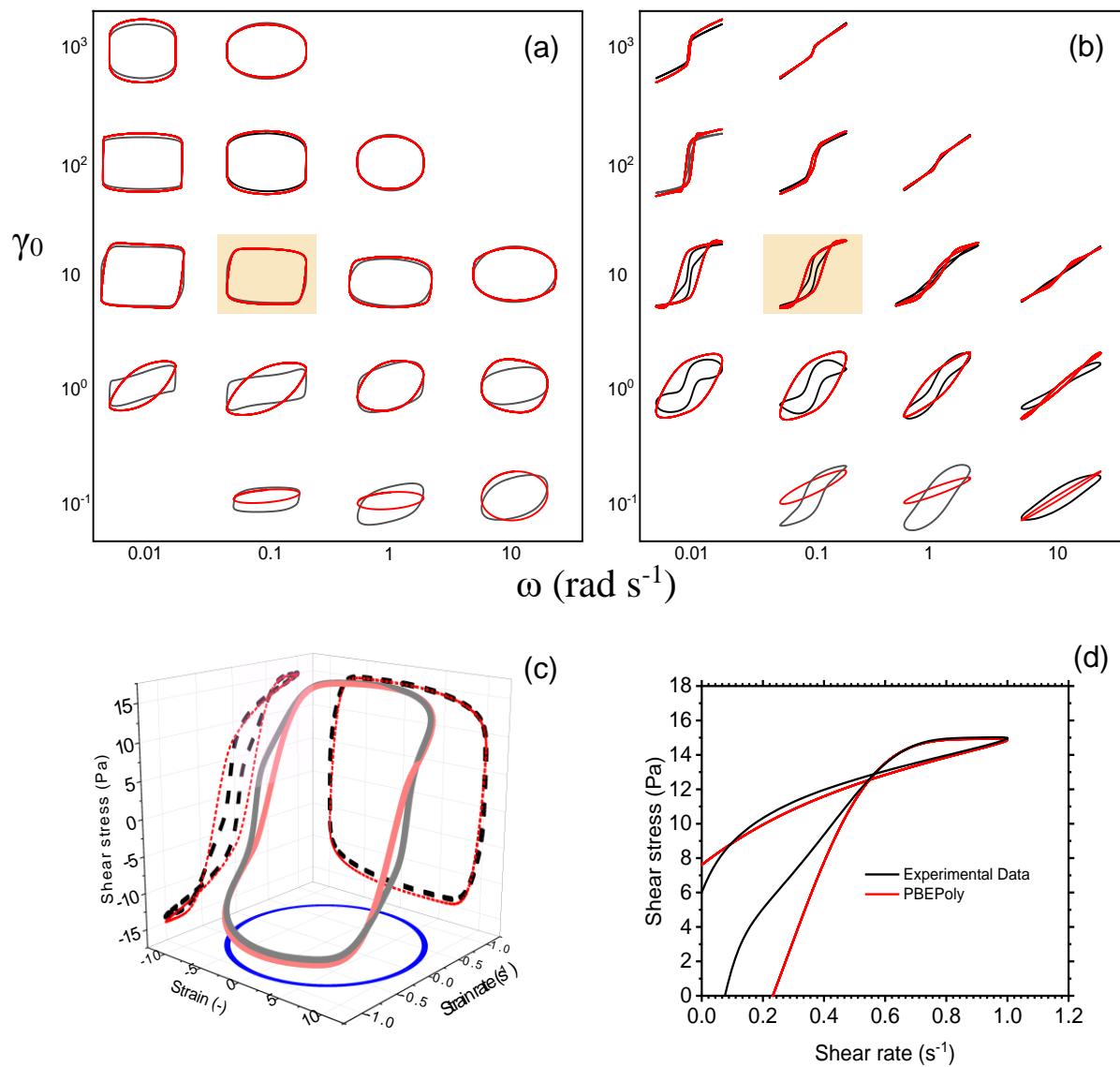


Figure 5 Comparison of model predictions (red line) with experimental measurements (black line, data after Armstrong *et al.*⁵¹) of large amplitude oscillatory shear measurements (LAOS) shown in the Pipkin space in terms of the elastic (a) and viscous (b) projections of Lissajous-Bowditch curves for a range of strain amplitudes and frequencies. (c) The projections highlighted in orange are plotted in three-dimensional space to illustrate the complete stress response with strain and strain rate. (d) A zoomed in view of the viscous projection.

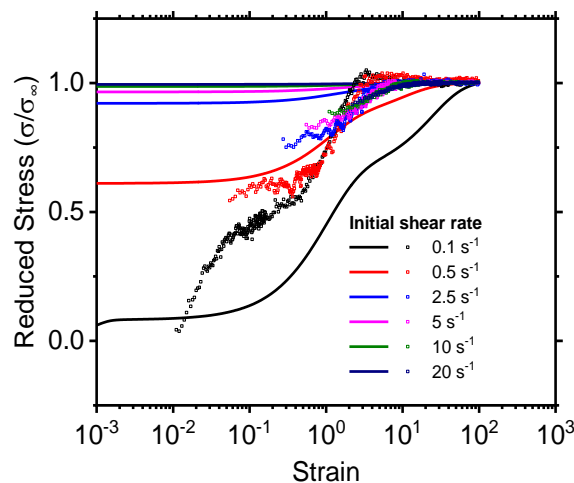


Figure 6 Flow reversal predictions (lines) for the fumed silica suspension of Wei *et al.*⁵² compared against experimental measurements (symbols). Note that flow reversal experiments were not explicitly included in the fitting as the parameters k_h and σ_{y0} were determined with small error bounds.

3.4. Discussion and suggestions for improvement

PBEPoly model fits and predictions confirm that polydispersity is critical for the accuracy of the steady state flow curve. After including polydispersity in the population balance formulation, the predictions for the agglomerate length scales become comparable to the values estimated from Rheo-uSANS. The monodisperse closure assumption (PBEMono) results in quantitatively inferior fits to the steady state data because it significantly overpredicts the agglomerate sizes. Improving the steady state fits naturally results in improved transients as well, illustrated through the step shear experiments and the LAOS predictions for a wide range of strain amplitudes and frequencies. Additionally, the predicted volume fraction reflects the high apparent volume fractions of polydisperse agglomerates.

Kinematic hardening does not play a role in experiments with unidirectional shearing protocols, such as steady shear flow sweeps and step transients. In LAOS and shear reversal on the other hand, kinematic hardening becomes necessary to capture the transients due to the Bauschinger

effect. The yield plane moves in the direction of applied flow and in the experiments where the flow direction changes, the yield plane undergoes a transient before it is established fully in the reverse direction. These transients are controlled by the back stress modulus k_h and the parameter q .

Although the shear rate involved in the shear aggregation and breakage kernels is corrected following Joshi's work,²⁵ there is still a need to reformulate these expressions such that they have implicit dependence on the invariants of applied stress. Because such a reformulation would require that the population balance equation depend on an internal variable (i.e. stress or conformation tensor) instead of the shear rate, not only will this ensure thermodynamic admissibility, but also make the model applicable for both stress-controlled and rate-controlled rheometric protocols without reparameterization. A theoretical skeleton for such a tensorial description can be generated using non-equilibrium thermodynamics, as shown by Jariwala *et al.*⁴⁹, though inferring the phenomenological parameters for generalized aggregation and breakage dynamics requires more development on the simulation and experimental front before this framework can be generalized beyond simple shear flows.

Another area where more work is needed to improve the PBEPoly model is the description of viscoelasticity. Although the transient fits are comparable to the ML-IKH structure kinetics model, the constitutive equation (Eq. (23)) overpredicts stress at low deformation rates and does not exhibit sharp transitions in elasticity. There are many phenomenological alternatives (SPTT-IKH model by Varchanis *et al.*²² and the rate-dependent relaxation proposed by Kamani *et al.*⁷²), yet developing one that is based on the detailed structural considerations remains to be examined from a more rigorous, microscopic point of view. Brownian dynamics simulations⁹¹ have been found to reveal the complex anisotropy and residual stresses that can develop within agglomerates. Such

simulations can help identify adequate structural descriptors to characterize back stress and dynamic yield stress in our model.

Recent machine learning tools have also been developed to learn constitutive models using rheological measurement data for systems that exhibit non-ideal/irreversible TEVP characteristics. The key limitation in such approaches is typically the lack of rheometry data available for a wide range of transients and deformation types. Using the results of a physics-based constitutive model, such as PBEPoly, to generate low-fidelity data in combination with a few high-quality experimental measurements to train Physics-Informed Neural Networks (PINNs) has been shown to be a promising approach by Mahmoudabadbozchelou and Jamali.^{92,93} Lennon *et al.*⁹⁴ have also demonstrated that one can incorporate fully-connected forward neural networks, that take stress and deformation tensors (along with their rates and gradients) as inputs, into a physics-based viscoelastic expression to construct data-driven constitutive models.

4. Conclusion

Improvements in the population balance modeling framework in terms of allowing for polydispersity and achieving thermodynamic consistency are successfully implemented and shown to improve model fits and predictions, including the ability to predict effect of mesoscale agglomeration and breakage processes on not only the macroscopic rheological behavior, but also the agglomerate fractal dimension and size. We have illustrated how this model can capture dynamic arrest, shear thinning, yield stress, kinematic hardening, and viscoelastic characteristics observed in aggregating suspensions using physically defined parameters that can be obtained or tested independently of fitting. In addition, we also showed the ability of this model to generate accurate structural descriptors, such as apparent volume fraction of agglomerates, mass mean radii, radii of gyration, that further enable incorporation of independent physical modeling of more complex

particle-level phenomena, such as diffusion and non-reversible restructuring and compaction without reparameterization of the model. The accuracy of population balance modeling can be further enhanced by including additional scaled integer moments, as needed.

The present scalar description is also thermodynamically consistent as the phenomenological constants in the model equations depend strictly on internal structural variables, borrowing from Joshi,²⁵ Souvaliotis and Beris⁴⁴ and Jariwala *et al.*⁴⁹ Although the current model already surmounts the empiricism involved in the structure kinetics framework and offers a quantitatively comparable and structurally-based alternative for scalar representation of stress, it stands to benefit from novel experiments, direct numerical simulation, and data-driven methods to further improve its predictive capabilities.

Conflict of Interest

Authors report no conflict of interest.

Acknowledgements

S.J., A.N.B. and N.J.W. gratefully acknowledge the support of the National Science Foundation (NSF) through the award CBET 1804911. J.H. and N.J.W. acknowledge the support of the National Institute of Standards and Technology, U.S. Department of Commerce, in providing the neutron research facilities used in this work under cooperative agreement # 370NANB17H302. This work utilized facilities supported in part by the National Science Foundation under Agreement No. DMR-0944772. The statements, findings, conclusions and recommendations are those of the authors and do not necessarily reflect the view of NSF, NIST, or the U.S. Department of Commerce.

Data availability

The experimental data and code used for this work can be obtained from the repository located at: <https://github.com/sohamjariwala/PBEPoly>.

Appendix A: Derivation of moment equations from the integro-differential form of the population balance equation

Each term in the integro-differential form of the population balance equation can be treated independently to evaluate its representation in the scaled moment space, μ_k . First, the number density is scaled with the total number of primary particles, N_0 ,

$$\hat{n}(m) = \frac{n(m)}{N_0},$$

such that the scaled moment, μ_k is defined as:

$$\mu_k \equiv \int_0^{\infty} m^k \hat{n}(m) dm.$$

Left hand side

$$\int_0^{\infty} m^k \frac{dn(m)}{dt} dm \Rightarrow \frac{d}{dt} \int_0^{\infty} m^k N_0 \hat{n}(m) dm = N_0 \frac{d\mu_k}{dt} \quad (31)$$

Shear aggregation terms

The k^{th} -moment of the birth and death terms corresponding to shear aggregation are:

$$\begin{aligned}
 SA_k &= \int_0^\infty m^k \left[\frac{1}{2} \int_0^m a(m-m', m'; \dot{\gamma}_p) n(m-m') n(m') dm' - \int_0^\infty a(m', m; \dot{\gamma}_p) n(m) n(m') dm' \right] dm \\
 &= N_0^2 \left[\frac{1}{2} \int_0^\infty \int_{m'}^\infty a(m-m', m'; \dot{\gamma}_p) m^k \hat{n}(m-m') \hat{n}(m') dm dm' \right. \\
 &\quad \left. - \int_0^\infty \int_0^\infty a(m', m; \dot{\gamma}_p) m^k \hat{n}(m) \hat{n}(m') dm' dm \right] \tag{32}
 \end{aligned}$$

Performing a change of variables, $m = p + m'$, such that

$$SA_k = N_0^2 \left[\frac{1}{2} \int_0^\infty \int_0^\infty a(p, m'; \dot{\gamma}_p) (p+m')^k \hat{n}(p) \hat{n}(m') dm dm' \right. \\
 \left. - \int_0^\infty \int_0^\infty a(m', m; \dot{\gamma}_p) m^k \hat{n}(m) \hat{n}(m') dm' dm \right], \tag{33}$$

and replacing p with m results in,

$$SA_k = N_0^2 \left[\frac{1}{2} \int_0^\infty \int_0^\infty a(m, m'; \dot{\gamma}_p) (m+m')^k \hat{n}(m) \hat{n}(m') dm' dm \right. \\
 \left. - \int_0^\infty \int_0^\infty a(m', m; \dot{\gamma}_p) m^k \hat{n}(m) \hat{n}(m') dm' dm \right]. \tag{34}$$

Using binomial expansion $(m+m')^k = \sum_{n=0}^k {}^k C_n m^{k-n} m'^n$ and substituting $a(m, m'; \dot{\gamma}_p)$ from Eq. (2)

, we get

$$SA_k = \frac{4}{3} \beta \alpha \alpha_p^3 |\dot{\gamma}_p| N_0^2 \left[\frac{1}{2} \sum_{n=0}^k {}^k C_n \int_0^\infty \int_0^\infty \left(m^{3/d_f} + 3m^{2/d_f} m'^{1/d_f} \right) m^{k-n} m'^n \hat{n}(m) \hat{n}(m') dm' dm \right. \\
 \left. - \int_0^\infty \int_0^\infty \left(m^{3/d_f} + 3m^{2/d_f} m'^{1/d_f} \right) m^k \hat{n}(m) \hat{n}(m') dm' dm \right], \tag{35}$$

which can be further simplified to,

$$SA_k = \frac{4}{3} \beta \alpha \alpha_p^3 |\dot{\gamma}_p| N_0^2 \left[\begin{array}{l} \frac{1}{2} \sum_{n=0}^k {}^k C_n \left(\mu_{k-n+3/d_f} \mu_n + 3\mu_{k-n+2/d_f} \mu_{n+1/d_f} \right) \\ + 3\mu_{k-n+1/d_f} \mu_{n+2/d_f} + \mu_{k-n} \mu_{n+3/d_f} \right) \\ - \left(\mu_{k-n+3/d_f} \mu_0 + 3\mu_{k-n+2/d_f} \mu_{1/d_f} \right) \\ + 3\mu_{k-n+1/d_f} \mu_{2/d_f} + \mu_{k-n} \mu_{3/d_f} \end{array} \right]. \quad (36)$$

Brownian aggregation terms

In Eq. (34), replacing $a(m, m'; \dot{\gamma}_p)$ with $c(m, m')$ and using the binomial expansion, we get

$$Br_k = N_0^2 \left[\begin{array}{l} \sum_{n=0}^k {}^n C_k \int_0^\infty \int_0^\infty c(m, m') m^{k-n} m'^n \hat{n}(m) \hat{n}(m') dm dm' \\ - \int_0^\infty \int_0^\infty c(m, m') m^k \hat{n}(m) \hat{n}(m') dm dm' \end{array} \right]. \quad (37)$$

On further simplification,

$$Br_k = \frac{2}{3} \frac{k_B T \beta}{\mu_s \eta_r W} N_0^2 \left[\begin{array}{l} \frac{1}{2} \sum_{k=0}^k {}^k C_n \left(\mu_{k-n+1/d_f} \mu_{n-1/d_f} + 2\mu_{k-n} \mu_n + \mu_{k-n-1/d_f} \mu_{n+1/d_f} \right) \\ - \left(\mu_{k+1/d_f} \mu_{-1/d_f} + 2\mu_0 \mu_k + \mu_{k-1/d_f} \mu_{1/d_f} \right) \end{array} \right] \quad (38)$$

Shear breakage terms

The shear breakage terms in the population balance equation (Eq. (1)) are:

$$SB_k = N_0 \int_0^\infty m^k \left[\int_m^\infty b(m'; \dot{\gamma}_p) P(m | m') \hat{n}(m') dm' - b(m; \dot{\gamma}_p) \hat{n}(m) \right] dm. \quad (39)$$

The moments of the daughter distribution $\hat{P}(\xi) \equiv m' P(m | m')$ are defined as $\theta_k = \int_0^1 \xi^k \hat{P}(\xi) d\xi$,

where $\xi = \frac{m}{m'}$, such that $d\xi = \frac{dm}{m'}$. Substituting in Eq. (39) gives,

$$\begin{aligned}
 SB_k &= N_0 \left[\int_0^\infty \int_0^1 (\xi m')^k b(m'; \dot{\gamma}_p) \hat{n}(m') P(m | m') m' d\xi dm' - \int_0^\infty b(m; \dot{\gamma}_p) m^k \hat{n}(m) dm \right] \\
 &= N_0 \left[\int_0^\infty m'^k b(m'; \dot{\gamma}_p) \hat{n}(m') \int_0^1 \xi^k P(\xi) d\xi dm' - \int_0^\infty b(m; \dot{\gamma}_p) m^k \hat{n}(m) dm \right] \\
 &= N_0 \left[\int_0^\infty m^k b(m; \dot{\gamma}_p) \hat{n}(m) dm (\theta_k - 1) \right].
 \end{aligned} \tag{40}$$

Now, substituting $b(m; \dot{\gamma}_p)$ gives,

$$\begin{aligned}
 SB_k &= b_0 \dot{\gamma}_p^2 (\theta_k - 1) N_0 \int_0^\infty \left(m^{1/d_f} - m_p^{1/d_{fpc}} \right) \hat{n}(m) m^k dm \\
 &= b_0 \dot{\gamma}_p^2 (\theta_k - 1) N_0 \left(\mu_{k+1/d_f} - m_p^{1/d_{fpc}} \mu_k \right).
 \end{aligned} \tag{41}$$

The final moment equation can be written as:

$$N_0 \frac{d\mu_k}{dt} = Br_k + SA_k + SB_k, \tag{42}$$

which simplifies to,

$$\begin{aligned}
 \frac{d\mu_k}{dt} &= \frac{2}{3} \frac{k_B T \beta}{\mu_s \eta_r W} N_0 \left[\frac{1}{2} \sum_{n=0}^k {}^k C_n \left(\mu_{k-n+1/d_f} \mu_{n-1/d_f} + 2\mu_{k-n} \mu_n + \mu_{k-n-1/d_f} \mu_{n+1/d_f} \right) \right. \\
 &\quad \left. - \left(\mu_{k+1/d_f} \mu_{-1/d_f} + 2\mu_0 \mu_k + \mu_{k-1/d_f} \mu_{1/d_f} \right) \right] \\
 &\quad + \frac{4}{3} \beta \alpha a_p^3 |\dot{\gamma}_p| N_0 \left[\frac{1}{2} \sum_{n=0}^k {}^k C_n \left(\mu_{k-n+3/d_f} \mu_n + 3\mu_{k-n+2/d_f} \mu_{n+1/d_f} \right) \right. \\
 &\quad \left. + 3\mu_{k-n+1/d_f} \mu_{n+2/d_f} + \mu_{k-n} \mu_{n+3/d_f} \right) \\
 &\quad \left. - \left(\mu_{k-n+3/d_f} \mu_0 + 3\mu_{k-n+2/d_f} \mu_{1/d_f} \right) \right. \\
 &\quad \left. - \left(+3\mu_{k-n+1/d_f} \mu_{2/d_f} + \mu_{k-n} \mu_{3/d_f} \right) \right] \\
 &\quad + b_0 \dot{\gamma}_p^2 (\theta_k - 1) \left(\mu_{k+1/d_f} - m_p^{1/d_{fpc}} \mu_k \right).
 \end{aligned} \tag{43}$$

Furthermore, the number density of primary particles N_0 can be rewritten in terms of the volume fraction of primary particles, ϕ_p as

$$N_0 = \frac{\phi_p}{\frac{4}{3}\pi a_p^3}, \quad (44)$$

leading to the equations (6)-(8).

Appendix B: Method of interpolative closure

The moment equations are an infinite set of simultaneous ordinary differential equations with terms involving the fractional moments of the size distribution. The interpolative closure rule performs a polynomial interpolation to approximate the missing moments. The normalized moments of the distribution are represented as

$$\ln \hat{\mu}_j = \sum_{k=0}^N c_k j^k, \quad (45)$$

which implies that the scaled moments are,

$$\ln \mu_j = c_0 (1-j) + \sum_{k=1}^N c_k (j^k - j). \quad (46)$$

Here, a new set of unknowns, c_k are introduced, which are the polynomial coefficients. The moment differential equations now require a change of variables to this new set of unknowns which can be performed simply through a matrix multiplication,

$$\underline{c} = \underline{\underline{A}}^{-1} \ln \underline{\mu}, \quad (47)$$

where, the vector \underline{c} and $\underline{\mu}$ are,

$$\underline{c} = \begin{bmatrix} c_0 \\ c_2 \\ c_3 \\ \vdots \\ c_N \end{bmatrix}; \ln \underline{\mu} = \begin{bmatrix} \ln \mu_0 \\ \ln \mu_2 \\ \ln \mu_3 \\ \vdots \\ \ln \mu_N \end{bmatrix}, \quad (48)$$

and the matrix $\underline{A}_{[N-1 \times N-1]}$ is obtained as,

$$\underline{A}_{[N-1 \times N-1]} = \begin{bmatrix} 1 & 0 & 0 & \dots & 0 \\ 2^0 - 1 & 2^2 - 2 & 2^3 - 2 & \dots & 2^N - 2 \\ 3^0 - 3 & 3^2 - 3 & 3^3 - 3 & \dots & 3^N - 3 \\ \vdots & \vdots & \vdots & \ddots & \vdots \\ N^0 - N & N^2 - N & N^3 - N & \dots & N^N - N \end{bmatrix}. \quad (49)$$

The inverse of this matrix can be stored in the memory at the beginning of every computation for efficiency. The time derivatives in moment equations can still be evaluated in the scaled moment space and converted to the coefficient space in before the solution step using,

$$\frac{dc_{[N-1]}}{dt} = \underline{A}_{[N-1 \times N-1]}^{-1} \frac{d \ln \underline{\mu}_{[N-1]}}{dt}. \quad (50)$$

Appendix C: Viscosity of polydisperse suspension

For a polydisperse suspension, the relative viscosity can be evaluated by decomposing the distribution into a ternary system using the quadrature weights and abscissa followed by applying a hydrodynamic function by Mwasame *et al.*³⁸⁻⁴⁰, defined as

$$f_u(\phi) = \ln(\eta_{r,\text{mono}}(\phi)), \quad (51)$$

where $\eta_{r,\text{mono}}(\phi)$ is a viscosity function for monodisperse suspension, which in this case is selected to be the Krieger-Dougherty equation. Using the ϕ_{D_1} , ϕ_{D_2} and ϕ_{D_3} determined from Eq. (16) and

the diameters, $D_1 < D_2 < D_3$ determined from the quadrature abscissas, the hydrodynamic function for the trimodal system is,

$$f_{tri} \equiv f_u \left(\beta_2 (\beta_1 \phi_{D_1} + \phi_{D_2}) + \phi_{D_3} \right) + f_u (\beta_1 \phi_{D_1} + \phi_{D_2}) (1 - \beta_2) + f_u (\phi_{D_1}) (1 - \beta_1). \quad (52)$$

The volume fractions are weighted by non-linear functions β_1 and β_2 which can be determined using the diameter ratios and volume fractions,

$$\beta \left(\frac{d_1}{d_2}, \phi_1, \phi_2 \right) \equiv \left[\left(\frac{d_1}{d_2} \right)^{0.18} \right]^{1 - \left(\frac{0.54 \phi_1}{0.54 \phi_1 + \phi_2} \right)}$$

$$\alpha^* = \frac{\beta \left(\frac{D_1}{D_3}, \frac{\phi_{D_1}}{\phi_{D_3}} \right) \phi_{D_2} D_2 + \left(1 - \beta \left(\frac{D_1}{D_3}, \frac{\phi_{D_1}}{\phi_{D_3}} \right) \right) \phi_{D_1} D_1}{\beta \left(\frac{D_1}{D_3}, \frac{\phi_{D_1}}{\phi_{D_3}} \right) \phi_{D_2} + \left(1 - \beta \left(\frac{D_1}{D_3}, \frac{\phi_{D_1}}{\phi_{D_3}} \right) \right) \phi_{D_1}} \quad (53)$$

$$\beta_1 \equiv \beta \left(\frac{D_1}{\alpha^*}, \phi_{D_1}, \phi_{D_2} + \phi_{D_3} \right)$$

$$\beta_2 = \beta \left(\frac{\alpha^*}{D_3}, \beta_1 \phi_{D_1} + \phi_{D_2}, \phi_{D_2} \right)$$

Appendix D: Distribution reconstruction

The normalized moments of the size distribution can be computed as,

$$\hat{\mu}_k = \frac{\mu_k}{\mu_0^{1-k} \mu_1^k}. \quad (54)$$

The moments can then be used in fit to probability density distributions. We found that the lognormal does an adequate job representing the size distribution at low and high shear rates, and does not suffer from singularity experienced at high shear rates (due to monodispersed primary clusters)

in more advanced reconstructions such as those proposed by Diemer *et al.*⁶⁰ that involve modified gamma distribution or fitting to modified Laguerre polynomial basis. Using just one parameter, $\hat{\mu}_2$, the normalized form of the lognormal distribution can be computed as

$$f(\ln x) d \ln x = \frac{1}{\sqrt{2\pi \ln \sigma_g}} \exp \left[-\frac{1}{2} \left(\frac{\ln x - \ln x_g}{\ln \sigma_g} \right)^2 \right] d \ln x, \quad (55)$$

where,

$$\begin{aligned} \ln \sigma_g &= \ln \hat{\mu}_2 \\ x_g &= \frac{1}{\sqrt{\hat{\mu}_2}}. \end{aligned} \quad (56)$$

When plotting the distributions, the weights are chosen to normalize the area under the curve to unity.

Nomenclature

Greek symbols

α	Collision efficiency
β	Cut-off function
γ	Shear strain
$\dot{\gamma}$	Shear strain rate
γ_0	Strain amplitude
$\dot{\gamma}_e$	Elastic component of shear strain rate
$\dot{\gamma}_p$	Plastic component of shear strain rate
η_r	Relative viscosity
θ_k	Moment of the daughter distribution
μ_k	k^{th} scaled moment of the distribution $n(m)$
$\hat{\mu}_k$	k^{th} normalized moment of the distribution $n(m)$
μ_s	Solvent viscosity
ξ	Daughter distribution parameter m/m'
σ	Shear stress

σ_y, σ_{y0}	Yield stress and yield stress parameter
τ	Relaxation time
ϕ_a	Apparent volume fraction of agglomerates
ϕ_p	Volume fraction of primary particles
ϕ_{pc}	Critical volume fraction corresponding to minimum agglomerate size
ϕ_{max}	Maximum packing fraction
ω	Frequency

Latin symbols

a_p	Radius of the primary particle
A	Back strain
b_0	Breakage constant
c_i	MOMIC coefficient space for the scaled moments
D_i	Diameters corresponding to quadrature
d_f, d_{fpc}	Fractal dimension of agglomerates and primary cluster
f	Hydrodynamic function
G_0	Equilibrium elastic modulus
k_h	Back stress modulus
K_R	Pre-factor for fractal scaling
m	Size (volume) of primary particles
$n(m, t)$	Distribution of agglomerate population size
n_d	Number of daughter fragments after breakage
N_0	Number density of primary particles
$P(m m')$	Probability of generating agglomerate of size m' when agglomerate of size m breaks
p	White-Metzner relaxation exponent
q	Back stress relaxation parameters
R_a	Radius of agglomerate (generated using mass mean)
R_h	Hydrodynamic radius
s_d	Daughter distribution size parameter
t	time
T	Temperature
W	Fuchs' stability ratio

References

1. Mewis J, Wagner NJ. *Colloidal Suspension Rheology*: Cambridge University Press; 2012.

2. Mewis J, Wagner NJ. Thixotropy. *Advances in Colloid and Interface Science*. 2009 2009;147-148:214-227.
3. Mewis J. Thixotropy - A General Review. *Journal of Non-Newtonian Fluid Mechanics*. 1979 1979;6(1):1-20.
4. Barnes HA. Thixotropy—a review. *Journal of Non-Newtonian Fluid Mechanics*. 1997-05 1997;70(1-2):1-33.
5. Barthel H, Dreyer M, Gottschalk-Gaudig T, Litvinov V, Nikitina E. Fumed Silica - Rheological Additive for Adhesives, Resins, and Paints. *Macromolecular Symposia*. 2002;187(1):573-584.
6. Joshi YM. Dynamics of Colloidal Glasses and Gels. *Annual Review of Chemical and Biomolecular Engineering*. 2014/06/07 2014;5(1):181-202.
7. Suman K, Joshi YM. Microstructure and Soft Glassy Dynamics of an Aqueous Laponite Dispersion. *Langmuir*. 2018;34(44):13079-13103.
8. Beris AN, Horner JS, Jariwala S, Armstrong MJ, Wagner NJ. Recent advances in blood rheology: a review. *Soft Matter*. 2021;17(47):10591-10613.
9. Hlaváček M. The influence of the acetabular labrum seal, intact articular superficial zone and synovial fluid thixotropy on squeeze-film lubrication of a spherical synovial joint. *Journal of Biomechanics*. 2002/10/01/ 2002;35(10):1325-1335.
10. Larson RG. Constitutive equations for thixotropic fluids. *Journal of Rheology*. 2015 2015;59(3):595-611.
11. Larson RG, Wei Y. A review of thixotropy and its rheological modeling. *Journal of Rheology*. 2019-05-01 2019;63(3):477.
12. Goodeve CF. A general theory of thixotropy and viscosity. *Transactions of the Faraday Society*. 1939;35(0):342-358.
13. Mujumdar A, Beris AN, Metzner AB. Transient phenomena in thixotropic systems. *Journal of Non-Newtonian Fluid Mechanics*. 2002-02-01 2002;102(2):157-178.
14. Dullaert K. *Constitutive equations for thixotropic dispersions* [Doctoral Dissertation]. Leuven: Departement Chemische Ingenieurstechnieken, Katholieke Universiteit; 2005.
15. Dullaert K, Mewis J. A structural kinetics model for thixotropy. *J. Non-Newtonian Fluid Mech.* 2006 2006;139:21-30.
16. Ramkrishna D. *Population Balances: Theory and Applications to Particulate Systems in Engineering*: Academic Press; 2000.
17. *Theory and Applications of Colloidal Suspension Rheology*. Cambridge: Cambridge University Press; 2021. Wagner NJ, Mewis J, eds. Cambridge Series in Chemical Engineering.
18. *IUPAC Compendium of Chemical Terminology*. Research Triangle Park, NC: IUPAC; 2009.
19. Agarwal M, Sharma S, Shankar V, Joshi YM. Distinguishing thixotropy from viscoelasticity. *Journal of Rheology*. 2021;65(4):663-680.
20. Jamali S, Mckinley GH, Armstrong RC. Microstructural Rearrangements and their Rheological Implications in a Model Thixotropic Elastoviscoplastic Fluid. *Physical Review Letters*. 2017 2017;118:048003.
21. Wei Y, Solomon MJ, Larson RG. A multimode structural kinetics constitutive equation for the transient rheology of thixotropic elasto-viscoplastic fluids. *Journal of Rheology*. 2018 2018;62(6):433-450.
22. Varchanis S, Makrigiorgos G, Moschopoulos P, Dimakopoulos Y, Tsamopoulos J. Modeling the rheology of thixotropic elasto-visco-plastic materials. *Journal of Rheology*. 2019;63(4):609-639.
23. Saramito P. A new constitutive equation for elastoviscoplastic fluid flows. *Journal of Non-Newtonian Fluid Mechanics*. 2007/08/30/ 2007;145(1):1-14.
24. Thien NP, Tanner RI. A new constitutive equation derived from network theory. *Journal of Non-Newtonian Fluid Mechanics*. 1977/07/01/ 1977;2(4):353-365.
25. Joshi YM. Thixotropy, nonmonotonic stress relaxation, and the second law of thermodynamics. *Journal of Rheology*. 2022-01-01 2022;66(1):111-123.

26. Mwasame PM, Beris AN, Diemer RB, Wagner NJ. A constitutive equation for thixotropic suspensions with yield stress by coarse-graining a population balance model. *AIChE Journal*. 2017-02 2017;63(2):517-531.
27. Smoluchowski Mv. Versuch einer mathematischen Theorie der Koagulationskinetik kolloider Lösungen. *Zeitschrift für Physikalische Chemie*. 1918-01-01 1918;92U(1).
28. Smoluchowski M. Drei Vorträge über Diffusion, Brownsche Molekularbewegung und Koagulation von Kolloidteilchen. *Physikalische Zeitschrift*. 1916;17:557-571, 587-599.
29. Taboadaserrano P, Taboada-Serrano P, Chin CJ, Tsouris C. Modeling aggregation of colloidal particles. *Current opinion in colloid & interface science*. 2005 2005;10(3-4):123-132.
30. Lebovka NI. Aggregation of Charged Colloidal Particles. In: Müller M, ed. *Polyelectrolyte Complexes in the Dispersed and Solid State I: Principles and Theory*. Berlin, Heidelberg: Springer Berlin Heidelberg; 2014:57-96.
31. Jullien R. The Application of Fractals to Colloidal Aggregation. *Croatica chemica acta*. 1992;65(2):215-235.
32. Lazzari S, Nicoud L, Jaquet B, Lattuada M, Morbidelli M. Fractal-like structures in colloid science. *Advances in Colloid and Interface Science*. 2016-09-01 2016;235:1-13.
33. Lattuada M, Zaccone A, Wu H, Morbidelli M. Population-balance description of shear-induced clustering, gelation and suspension viscosity in sheared DLVO colloids. *Soft Matter*. 2016-06-15 2016;12(24):5313-5324.
34. Lattuada M, Wu H, Morbidelli M. A simple model for the structure of fractal aggregates. *Journal of Colloid and Interface Science*. 2003 2003.
35. Selomulya C, Bushell G, Amal R, Waite TD. Understanding the role of restructuring in flocculation: The application of a population balance model. *Chemical Engineering Science*. 2003/01/01/ 2003;58(2):327-338.
36. Jariwala S, Horner JS, Wagner NJ, Beris AN. Application of population balance-based thixotropic model to human blood. *Journal of Non-Newtonian Fluid Mechanics*. 07/2020 2020;281:104294.
37. Hipp JB, Richards JJ, Wagner NJ. Direct measurements of the microstructural origin of shear-thinning in carbon black suspensions. *Journal of Rheology*. 2021-03-01 2021;65(2):145-157.
38. Mwasame PM, Mertz CA, Rosario EJ, Beris AN, Wagner NJ. An experimental study of multimodal glass suspension rheology to test and validate a polydisperse suspension viscosity model. *Rheologica Acta*. 2017.
39. Mwasame PM, Wagner NJ, Beris AN. Modeling the effects of polydispersity on the viscosity of noncolloidal hard sphere suspensions. *Journal of Rheology*. 2016 2016;60:225.
40. Mwasame PM, Wagner NJ, Beris AN. Modeling the viscosity of polydisperse suspensions: Improvements in prediction of limiting behavior. *Physics of Fluids*. 2016 2016;28(6):61701.
41. Diemer RB, Olson J. A moment methodology for coagulation and breakage problems : Part 2 — moment models and distribution reconstruction. *Chemical Engineering Science*. 2002 2002;57:2211-2228.
42. Diemer RB, Olson J. A moment methodology for coagulation and breakage problems : Part 1 — analytical solution of the steady-state population balance. *Chemical Engineering Science*. 2002 2002;57:2193-2209.
43. Diemer RB, Olson J. A moment methodology for coagulation and breakage problems: Part 3 — generalized daughter distribution functions. *Chemical Engineering Science*. 2002 2002;57(19):4187-4198.
44. Souvaliotis A, Beris AN. An extended White–Metzner viscoelastic fluid model based on an internal structural parameter. *Journal of Rheology*. 1992-02-01 1992;36(2):241-271.
45. Beris AN, Edwards BJ. *Thermodynamics of Flowing Systems: with internal Microstructure*: Oxford University Press; 1994.
46. Bhattacharyya T, Jacob AR, Petekidis G, Joshi YM. On the nature of flow curve and categorization of thixotropic yield stress materials. *Journal of Rheology*. 2023;67(2):461-477.

47. Stephanou PS, Georgiou GG. A nonequilibrium thermodynamics perspective of thixotropy. *J. Chem. Phys.* 2018 2018:11.
48. Tsimouri IC, Stephanou PS, Mavrantzas VG. A constitutive rheological model for agglomerating blood derived from nonequilibrium thermodynamics. *Physics of Fluids*. 2018-03-01 2018;30(3):030710.
49. Jariwala S, Wagner NJ, Beris AN. A Thermodynamically Consistent, Microscopically-Based, Model of the Rheology of Aggregating Particles Suspensions. *Entropy*. 2022;24(5):717.
50. Stephanou PS. A constitutive hemorheological model addressing both the deformability and aggregation of red blood cells. *Physics of Fluids*. 2020-10-01 2020;32(10):103103.
51. Armstrong MJ, Beris AN, Rogers SA, Wagner NJ. Dynamic shear rheology of a thixotropic suspension: Comparison of an improved structure-based model with large amplitude oscillatory shear experiments. *Journal of Rheology*. 2016 2016;60:433.
52. Wei Y, Solomon MJ, Larson RG. Quantitative nonlinear thixotropic model with stretched exponential response in transient shear flows. *Journal of Rheology*. 2016;60(6):1301-1315.
53. Mwasame PM. *Multiscale modeling of fundamental rheological phenomena in particulate suspensions based on flow-microstructure interactions* [Doctoral Dissertation], University of Delaware; 2017.
54. Spicer PT, Pratsinis SE. Coagulation and fragmentation: Universal steady-state particle-size distribution. *AIChE Journal*. 1996/06/01 1996;42(6):1612-1620.
55. Ren Z, Harshe YM, Lattuada M. Influence of the Potential Well on the Breakage Rate of Colloidal Aggregates in Simple Shear and Uniaxial Extensional Flows. *Langmuir*. 2015-06-02 2015;31(21):5712-5721.
56. Harshe YM, Lattuada M. Breakage Rate of Colloidal Aggregates in Shear Flow through Stokesian Dynamics. *Langmuir*. 2012-01-10 2012;28(1):283-292.
57. Mohtaschemi M, Puisto A, Illa X, Alava MJ. Rheology dynamics of aggregating colloidal suspensions. *Soft Matter*. 2014;10(17):2971-2981.
58. Farr RS. Random close packing fractions of lognormal distributions of hard spheres. *Powder Technology*. 2013;245:28-34.
59. Farr RS, Groot RD. Close packing density of polydisperse hard spheres. *The Journal of Chemical Physics*. 2009-12-28 2009;131(24):244104.
60. Diemer RB, Olson JH. A moment methodology for coagulation and breakage problems: Part 2—moment models and distribution reconstruction. *Chemical Engineering Science*. 2002/06/01/ 2002;57(12):2211-2228.
61. Joshi YM. A model for aging under deformation field, residual stresses and strains in soft glassy materials. *Soft Matter*. 2015;11(16):3198-3214.
62. Shih W-H, Shih WY, Kim S-I, Liu J, Aksay IA. Scaling behavior of the elastic properties of colloidal gels. *Physical Review A*. 1990;42(8):4772--4779.
63. Armstrong PJ, Frederick CO. A Mathematical Representation of the Multiaxial Bauschinger Effect. *Materials at High Temperatures*. 2007;24(1):1-26.
64. Dimitriou CJ, McKinley GH. A canonical framework for modeling elasto-viscoplasticity in complex fluids. *Journal of Non-Newtonian Fluid Mechanics*. 2019/03/01/ 2019;265:116-132.
65. Wei Y, Solomon MJ, Larson RG. A multimode structural kinetics constitutive equation for the transient rheology of thixotropic elasto-viscoplastic fluids. *Journal of Rheology*. 2018;62(1):321-342.
66. Krieger IM, Dougherty TJ. A Mechanism for Non-Newtonian Flow in Suspensions of Rigid Spheres. *Transactions of the Society of Rheology*. 1959 1959;3:137.
67. Maron SH, Pierce PE. Application of ree-yring generalized flow theory to suspensions of spherical particles. *Journal of Colloid Science*. 1956-02-01 1956;11(1):80-95.
68. Quemada D. Rheological modelling of complex fluids. I. The concept of effective volume fraction revisited. *The European Physical Journal - Applied Physics*. 1998;1(1):119-127.

69. Quemada D. Rheology of concentrated disperse systems II. A model for non-newtonian shear viscosity in steady flows. *Rheologica Acta*. 1978;17(6):632-642.
70. Gordon RG. Error Bounds in Equilibrium Statistical Mechanics. *Journal of Mathematical Physics*. 1968;9(5):655-663.
71. McGraw R. Description of Aerosol Dynamics by the Quadrature Method of Moments. *Aerosol Science and Technology*. 1997;27(2):255-265.
72. Kamani K, Donley GJ, Rogers SA. Unification of the Rheological Physics of Yield Stress Fluids. *Physical Review Letters*. 05/25/ 2021;126(21):218002.
73. Oldroyd JG. A rational formulation of the equations of plastic flow for a Bingham solid. *Mathematical Proceedings of the Cambridge Philosophical Society*. 1947;43(1):100-105.
74. Hohenemser K, Prager W. Über die Ansätze der Mechanik isotroper Kontinua. *ZAMM - Zeitschrift für Angewandte Mathematik und Mechanik*. 1932;12(4):216-226.
75. Perzyna P. Thermodynamic Theory of Viscoplasticity. In: Yih C-S, ed. *Advances in Applied Mechanics*. Vol 11: Elsevier; 1971:313-354.
76. Awad TS, Rogers MA, Marangoni AG. Scaling Behavior of the Elastic Modulus in Colloidal Networks of Fat Crystals. *Journal of Physical Chemistry*. 2004;108(1):171-179.
77. Marangoni AG. Elasticity of high-volume-fraction fractal aggregate networks: A thermodynamic approach. *Physical Review B*. 2000-12-01 2000;62(21):13951-13955.
78. Babick F. Suspensions of Colloidal Aggregates. *Suspensions of Colloidal Particles and Aggregates*: Springer International Publishing; 2016:119-220.
79. Armstrong MJ, Beris AN, Wagner NJ. An adaptive parallel tempering method for the dynamic data-driven parameter estimation of nonlinear models. *AIChE Journal*. 2017-06-01 2017;63(6):1937-1958.
80. Armstrong MJ, Beris AN, Rogers SA, Wagner NJ. Dynamic shear rheology and structure kinetics modeling of a thixotropic carbon black suspension. *Rheologica Acta*. 2017-10-05 2017;56(10):811-824.
81. Wang Y, Ewoldt RH. New insights on carbon black suspension rheology—Anisotropic thixotropy and antithixotropy. *Journal of Rheology*. 2022/09/01 2022;66(5):937-953.
82. Hipp JB, Richards JJ, Wagner NJ. Structure-property relationships of sheared carbon black suspensions determined by simultaneous rheological and neutron scattering measurements. *Journal of Rheology*. 2019 2019;63:423.
83. Richards JJ, Hipp JB, Riley JK, Wagner NJ, Butler PD. Clustering and Percolation in Suspensions of Carbon Black. *Langmuir*. 2017-10-31 2017;33(43):12260-12266.
84. Pashminehazar R, Kharaghani A, Tsotsas E. Determination of fractal dimension and prefactor of agglomerates with irregular structure. *Powder Technology*. 2019-02-01 2019;343:765-774.
85. Bantawa M, Keshavarz B, Geri M, et al. The hidden hierarchical nature of soft particulate gels. 2022. <https://arxiv.org/abs/2211.03693>.
86. Donley GJ, de Bruyn JR, McKinley GH, Rogers SA. Time-resolved dynamics of the yielding transition in soft materials. *Journal of Non-Newtonian Fluid Mechanics*. 2019/02/01/ 2019;264:117-134.
87. Rogers SA. In search of physical meaning: defining transient parameters for nonlinear viscoelasticity. *Rheologica Acta*. 2017/05/01 2017;56(5):501-525.
88. Dimitriou CJ, Ewoldt RH, Mckinley GH. Describing and prescribing the constitutive response of yield stress fluids using large amplitude oscillatory shear stress (LAOStress). *Journal of Rheology*. 2013 2013;57:27.
89. Hyun K, Wilhelm M, Klein CO, et al. A review of nonlinear oscillatory shear tests: Analysis and application of large amplitude oscillatory shear (LAOS). *Progress in Polymer Science*. 12/2011 2011;36(12):1697-1753.
90. Armstrong M, Pincot A, Jariwala S, Horner J, Wagner N, Beris A. Tensorial formulations for improved thixotropic viscoelastic modeling of human blood. *Journal of Rheology*. 2022-03-01 2022;66(2):327-347.

91. Moghimi E, Jacob AR, Petekidis G. Residual stresses in colloidal gels. *Soft Matter*. 2017;13(43):7824-7833.
92. Mahmoudabadbozchelou M, Caggioni M, Shahsavari S, Hartt WH, Em Karniadakis G, Jamali S. Data-driven physics-informed constitutive metamodelling of complex fluids: A multifidelity neural network (MFNN) framework. *Journal of Rheology*. 2021;65(2):179-198.
93. Mahmoudabadbozchelou M, Jamali S. Rheology-Informed Neural Networks (RhINNs) for forward and inverse metamodelling of complex fluids. *Scientific Reports*. 2021;11(1).
94. Lennon KR, McKinley GH, Swan JW. Scientific Machine Learning for Modeling and Simulating Complex Fluids. 2022;2210.04431v1. <https://dx.doi.org/10.48550/arxiv.2210.04431>.